CHAPTER 6

Biologically active cholesterol-based thiazole derivatives

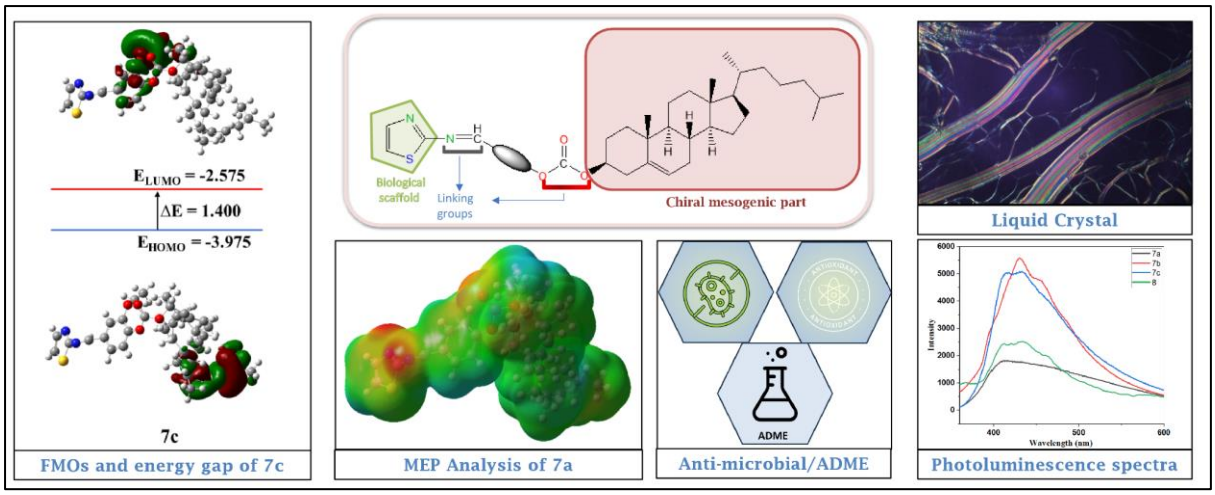

6.1. Introduction

In medicinal chemistry, heterocyclic molecules showing biological activities are extremely important. Many physiologically active compounds have cyclic organic frameworks, particularly heterocyclic frameworks. These compounds have been synthesized or extracted from plants and have shown antifungal, anti-inflammatory, and other biological activities [1]. Heterocycles are utilized in the pesticide, medicinal, and veterinary industries, as well as for corrosion inhibition, antioxidants, dyestuffs, copolymers etc. [2]. For medicinal chemists, heterocycles are crucial because they can expand the chemical space that can be used to make a variety of biologically active heterocycles having wide range of activities, including anti-cancer, anti-depressant, anxiolytic, anti-microbial, anti-oxidant enzyme inhibition, anti-inflammatory, and many more.

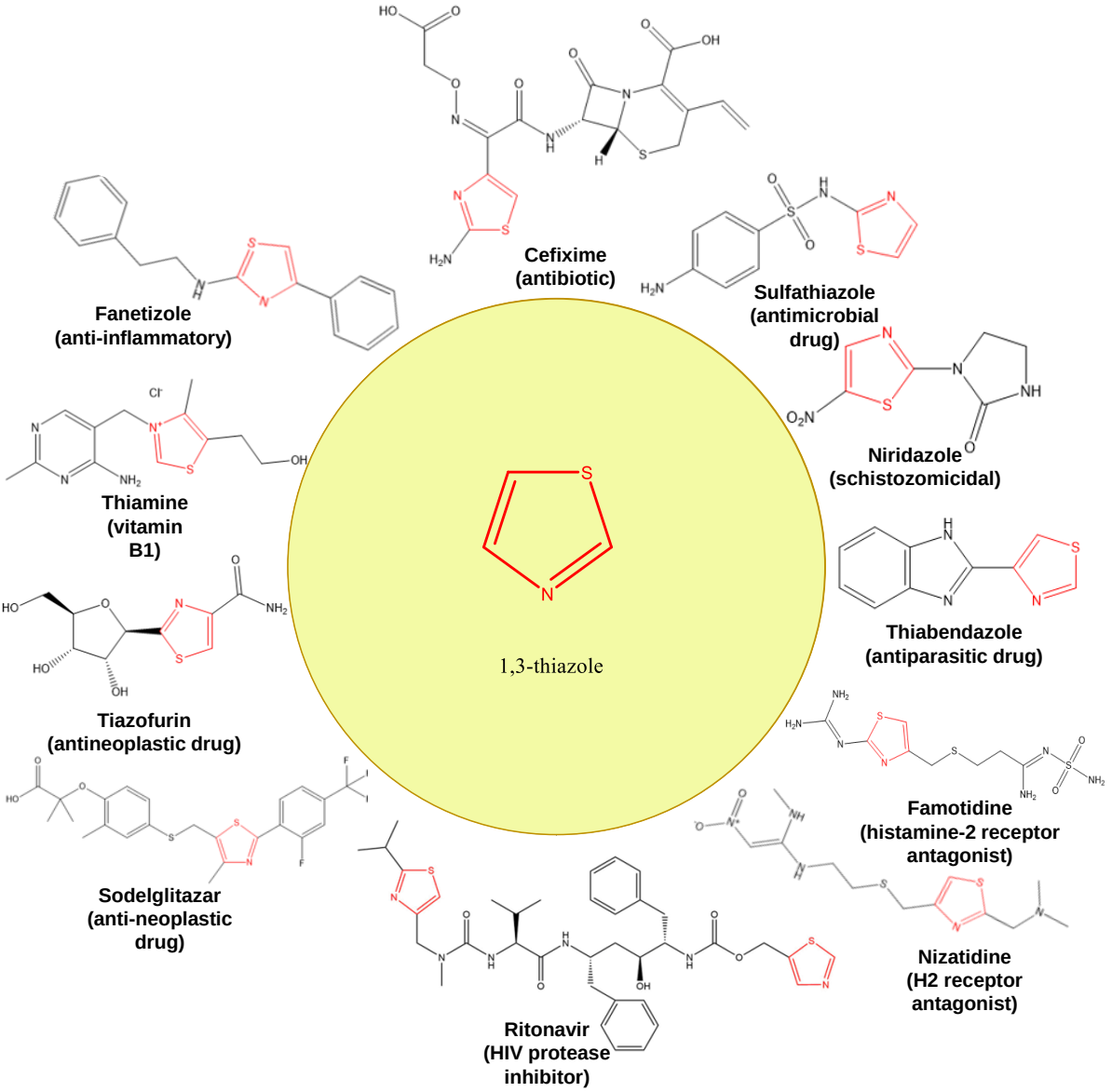

Figure 6.1: Some commercially available drugs containing thiazole moiety

Heterocycles can be utilized to alter characteristics including solubility, lipophilicity, polarity, and hydrogen bonding capability of physiologically active compounds, enhances the ADME/Tox properties of drugs or potential therapeutic candidates [3]. Heterocyclic compounds containing nitrogen atoms are widely acknowledged as the most abundant category of chemical constituents comprising biologically active complexes, natural products, and chemicals often utilized in medicinal chemistry [4,5].

In addition to studying nitrogen heteroatom-based heterocycles extensively, scientists have also demonstrated a significant interest in other heterocycles, such as sulphur-containing heterocyclic molecules. [6,7]. These chemicals have demonstrated a diverse range of biological actions. Sulphur-containing heterocycles are found in several FDA-approved medications, including clopidogrel and ticlopidine for the prevention of blood clots, raloxifene to treat breast cancer, and rosiglitazone and pioglitazone in the treatment of diabetes, etc. [8]. Similarly, Ritonavir is an antiviral that is an HIV protease inhibitor [9]. Tolnaftate is a squalene epoxidase inhibitor used topically to treat fungal infections [10].

Thiazoles have significant biological uses, initially documented by Hantzsch and Weber in 1887 [11]. They have analogous chemical and physical characteristics to pyridine as well as pyrimidine, with some derivatives bearing resemblance to thiophene and furan. Nitrogen is identified as the most negatively polarized atom in molecular electrostatic potential (MEP) study, whereas carbon and sulfur are seen to stay electrically neutral [12]. In number of studies thiazole-based compounds have shown to possess good anti-microbial, anti-HIV, anti-inflammatory, anti-neoplastic, anti-ulcer etc. [13]. Amino thiazole and Schiff's base derived from amino-thiazole have shown promising results for new biologically active compounds **(Figure 6.1)** [14]. Thaizole based liquid crystalline derivatives have been studied but to a limited amount. Despite the fact that thiazoles are commonly found in published works, the scope of structural modifications that have been examined is still rather limited. A limited amount of work has been done on thiazole-based liquid crystalline compounds.

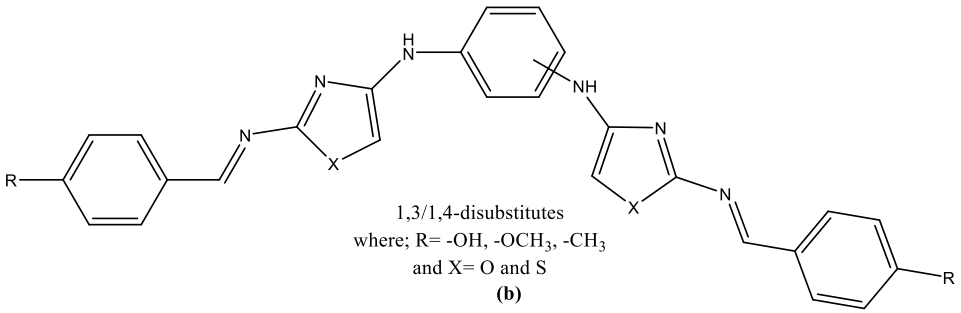

Figure 6.2 (a): Molecular structure of 1,3-thiazole based LC

T. K. Ibraheem et. al.[15] **(Figure 6.2 (a))**, have synthesized oxazole and 1,3-thiazole based liquid crystals, where the oxazole derivatives displayed purely smectic A mesophases in contrast to the thiazole which exhibited enantiotropic nematic mesophases.

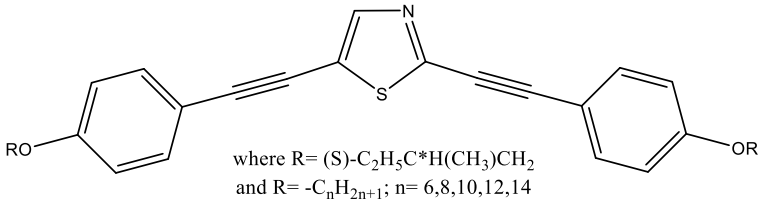

(a)

Figure 6.2 (b): Molecular structure of 1,3-thiazole based LC with terminal alkyl chains

C.H. Lee et al. [16] **(Figure 6.2 (b))**, reported bent core thiazole derivatives with terminal alkyl chains, exhibiting nematic and smectic A mesophases. Also, in one compound, the terminal alkyl chain was substituted with a chiral chain, and it was found that the compound exhibited a smectic C* phase.

Also, some other thiazole-based LCs have been synthesized showing variety of mesophases and fluorescent behaviour [17–19].

Cholesterol derivatives have strong antimicrobial properties as well as other biological properties including anti-cancer and antioxidant effects. Cholesterol-based compounds have several applications such as in liquid crystal, drug delivery, gelators and other synthetic uses [20].

This study describes the synthesis and analysis of some Schiff's base compounds derived from amino thiazole and various substituted formyl phenyl cholesteryl carbonates. We have also investigated their mesomorphic as well as photoluminescence properties and evaluated their biological activities. Also, DFT studies have been carried out including frontier MOs and MEP analysis.

6.2. Experimental details

6.2.1. Materials

Cholesteryl chloroformate and 2-amino thiazole was purchased from Sigma-Aldrich Chemicals, USA. 1,1-Diphenyl-2-picrylhydrazyl (for antioxidant assay) was purchase from TCI chemicals, Japan. 4-Hydroxybenzaldehyde, salicylaldehyde, 4-hydroxy-3-methoxybenzaldehyde, 4-hydroxy-3-ethoxybenzaldehyde, anhydrous pyridine, glacial acetic acid, chloroform, ethyl acetate, n-hexane and other reagents were procured from “Loba Chemie Pvt. Ltd., India”. Tetrahydrofuran and methanol were subjected to drying treatment using

standard techniques. All the other solvents and reagents were of analytical reagent grade and were used as received.

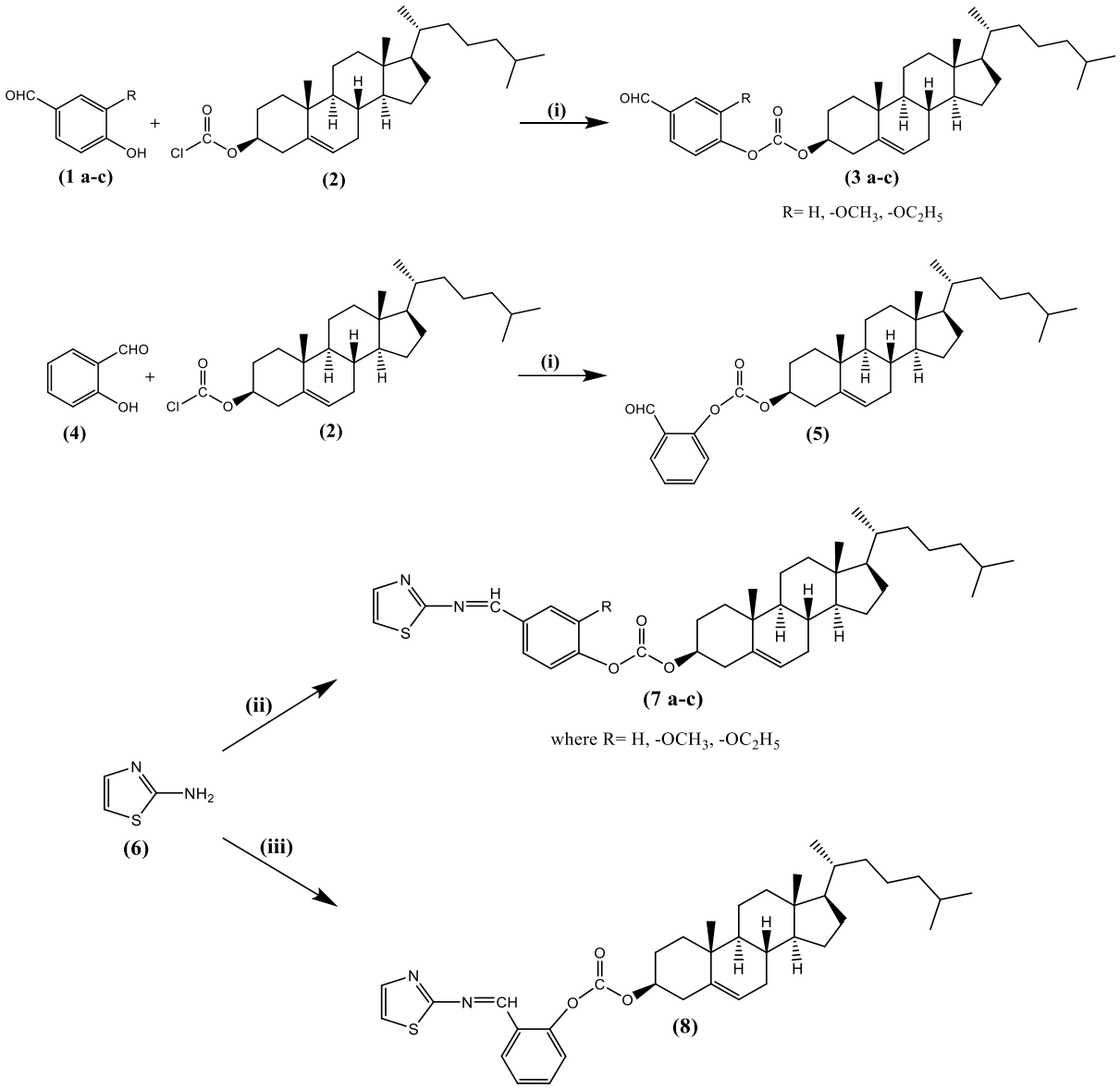

Scheme 6.1: Synthetic pathway for synthesizing the final Schiff's bases. **(7a-c)** and **(8)**. Reagents and conditions; (i) dry tetrahydrofuran, anhy. pyridine, continuous stirring at 38-40°C, 3-4 h; (ii) **(3a-c)**, $CHCl_3$: MeOH (1:1), glacial HAc, 10-12 h; (iii) **(5)**, $CHCl_3$: MeOH (1:1), glacial HAc, 10-12 h.

6.2.2. Techniques and measurements

The synthetic pathway used is shown in Scheme 6.1. The compounds' structures were identified by conventional spectroscopic techniques. TLC was conducted using silica gel plates from Merck. FT-IR spectra were obtained using a Bruker spectrometer with KBr Pellets. ^{1}H-NMR and ^{13}C-NMR spectra were obtained using a 400 MHz Avance Bruker spectrometer.

Deuterated chloroform ($CDCl_3$) was used as the solvent, while TMS served as the internal standard. The polarised optical microscopy (POM) study was observed with a Nikon Eclipse Ci-Pol microscope equipped with a Linkam (Linkam, Surrey, England) heating stage. Phase transition temperatures and thermodynamic parameters were determined by using differential scanning calorimetry (DSC-822, Mettler Toledo, having Stare software). The heating as well as cooling rates were 10°C min^{-1}. The compounds' thermal stability was assessed using a thermogravimetry analyzer (TGA-50, Shimadzu, Japan) with 3-7 mg of the sample in a platinum pan, heated at a rate of 10°C min^{-1}. An elemental analysis was conducted using Thermo Finnigan's CHN analyzer using the Flash 1112 series EA. The absorbance was measured using a Shimadzu UV-1800 spectrophotometer from Japan. Photoluminescence and quantum yields (Φ_{PL}) were measured using a Shimadzu RF 6000 Spectrofluorophotometer (Japan). Gaussian 09, revision A.02 software was utilized for DFT calculations.

6.2.3. Synthesis and characterization

*6.2.3.1. General procedure for the synthesis of formyl phenyl cholesteryl carbonates **(3a-c/5)***

Formyl phenyl cholesteryl carbonates were synthesized using previously reported method [21]. Cholesteryl chloroformate **(2) (**0.01 mol) and 50 ml dry THF were added to RBF. The contents were rapidly mixed with 4-hydroxy-3-substituted benzaldehyde **(1a-c)** / salicylaldehyde **(4) (**0.012 mol), 4.0 ml of anhy. pyridine as proton scavenger and an additional 40 ml dry THF was added to the reaction mixture and stirring was continued for 3-4 h at about 38-40 °C. Thereafter, mixture was filtered to isolated the precipitates of pyridinium chloride as well as other insoluble materials. The filtrate was concentrated using a vacuum in order to remove extra THF, then n-hexane was added to precipitate the product, filtered and recrystallized from ethyl acetate-methanol mixture till constant transition temperature were obtained.

Compound 3a: White crystalline solid, yield 66%; phase transition temperatures: Cr 139.0 °C N* 188.9 °C Iso 171.8 °C N* 116 °C Cr; IR (KBr, ν_{max}, cm^{-1}): 3034, 2943, 2888, 2868, 2851, 2790, 2720, 1755, 1703, 1600, 1502, 839; ^{1}H-NMR ($CDCl_3$, 400 MHz): δ (ppm) = 9.91 (s, 1H, -CHO), 7.94-7.92 (d, 2H, J = 8.8 Hz, Ar-H), 7.32-7.30 (d, 2H, J = 8.8 Hz, Ar-H), 5.46-5.44 (m, 1H, -C=CH-), 4.66-4.58 (m, 1H, -OC<u>H</u>-CH_2-), 2.52-2.50 (q, 2H, -OCH-C<u>H_2</u>-), 2.05-0.70 (m, 41H, -CH, -CH_2 and -CH_3); ^{13}C NMR ($CDCl_3$, 400MHz): δ(ppm) = 191.20 (-CHO), 158.36, 150.10 (-O-COO-), 158.36, 139.08, 134.19, 129.75, 122.22, 121.44, 79.13,

56.69, 56.13, 49.98, 42.33, 39.71, 39.53, 37.94, 36.84, 36.57, 36.19, 35.81, 31.92, 31.84, 28.24, 28.04, 27.65, 24.30, 23.84, 22.85, 22.58, 21.06, 19.30, 18.72, 11.83; Elemental analysis: calculated for $C_{35}H_{50}O_4$ (%): C, 78.61; H, 9.42; found: C, 78.58, H; 9.46.

Compound 3b: White crystalline solid, yield 72%; phase transition temperatures: Cr 204.3 °C Iso 175.4 °C N* 78.2 °C; IR (KBr, ν_{max}, cm^{-1}): 3039, 2943, 2889, 2868, 2851, 2793, 2736, 1763, 1701, 1602, 1504, 842; ^{1}H-NMR ($CDCl_3$, 400 MHz): δ (ppm) = 9.84 (s, 1H, -CHO), 7.34-7.32 (d, 1H, J = 8.8 Hz, Ar-H), 7.26-7.24 (d, 1H, J = 8.8 Hz, Ar-H), 6.29 (s, 1H, Ar-H), 5.46-5.44 (m, 1H, -C=CH-), 4.64-4.56 (m, 1H, -OC<u>H</u>-CH_2-), 3.87 (s, 3H, -OCH_3), 2.52-2.49 (q, 2H, -OCH-C<u>H_2</u>-), 2.05-0.70 (m, 41H, -CH, -CH_2 and -CH_3); ^{13}C NMR ($CDCl_3$, 400MHz): δ(ppm) = 190.8 (-CHO), 154.45, 152.20 (-O-COO-), 144.51, 139.04, 134.19, 129.78, 124.40, 122.40, 121.28, 114.05, 79.01, 58.20, 56.60, 56.14, 49.98, 42.32, 39.74, 39.57, 37.94, 36.88, 36.56, 36.18, 35.81, 31.94, 31.88, 28.29, 28.08, 27.65, 24.30, 23.84, 22.90, 22.55, 21.06, 19.31, 18.73, 11.82; Elemental analysis calculated for $C_{36}H_{52}O_5$ (%): C, 76.56; H, 9.28; found: C, 76.51, H; 9.23.

Compound 3c: White-crystalline solid, yield 76%; melting point (m.p.) = 144.5 °C; IR (KBr, ν_{max}, cm^{-1}): 3036, 2947, 2902, 2868, 2850, 2789, 2733, 1763, 1703, 1600, 1506, 839; ^{1}H-NMR ($CDCl_3$, 400 MHz): δ (ppm) = 9.66 (s, 1H, -CHO), 7.37-7.35 (d, 1H, J = 8.6 Hz, Ar-H), 7.25-7.23 (d, 1H, J = 8.6 Hz, Ar-H), 7.01 (s, 1H, Ar-H), 5.46-5.44 (m, 1H, -C=CH-), 4.64-4.56 (m, 1H, -OC<u>H</u>-CH_2-), 4.13 (q, 2H, -OC<u>H_2</u>-CH_3), 2.52-2.49 (q, 2H, -OCH-C<u>H_2</u>-), 2.08-0.70 (m, 44H, -CH, -CH_2 and -CH_3); ^{13}C NMR ($CDCl_3$, 400MHz): δ(ppm) = 191.0 (-CHO), 154.42, 150.0 (-O-COO-), 139.81, 134.22, 124.16, 123.32, 121.8, 113.20, 78.20, 64.06, 52.51, 51.80, 42.34, 39.78, 39.50, 37.90, 36.82, 36.53, 36.18, 35.81, 31.92, 31.80, 28.34, 28.13, 27.65, 24.34, 23.80, 22.90, 22.55, 21.06, 19.33, 18.76, 11.82; Elemental analysis: calculated for $C_{37}H_{54}O_5$ (%): C, 76.78; H, 9.40; found: C, 78.72, H; 9.46.

Compound 5: White-crystalline solid, yield 62%; melting point (m.p.) = 166.0 °C, IR (KBr, ν_{max}, cm^{-1}): 3079, 2952, 2933, 2868, 2852, 2768, 2722, 1791, 1732, 1604, 1511, 846; ^{1}H-NMR ($CDCl_3$, 400 MHz): δ (ppm) = 10.16 (s, 1H, -CHO), 7.91 (t, 1H, Ar-H), 7.52 (d, 1H, J = 18 Hz, Ar-H), 7.42 (d, 1H, J = 20 Hz, Ar-H), 7.12 (d, 1H, 20 Hz, Ar-H), 5.46-5.44 (m, 1H, -C=CH-), 4.64-4.56 (m, 1H, -OC<u>H</u>-CH_2-), 2.53-2.50 (q, 2H, -OCH-C<u>H_2</u>-), 2.08-0.70 (m, 44H, -CH, -CH_2 and -CH_3); ^{13}C NMR ($CDCl_3$, 400MHz): δ(ppm) = 191.04 (-CHO), 153.62, 150.02 (-O-COO-), 139.80, 134.94, 130.36, 126.03, 121.85, 120.54, 78.24, 52.55, 51.78, 42.34, 39.71, 39.54, 37.84, 36.74, 36.47, 36.09, 35.71, 31.84, 31.75, 28.23, 28.14, 27.65, 24.32, 23.84, 22.85, 22.58,22.50, 21.06, 19.31, 18.98, 14.14, 11.88; Elemental analysis: calculated for $C_{35}H_{50}O_4$ (%): C, 78.61; H, 9.42; found: C, 78.70, H; 9.44.

*6.2.3.2. General procedure for the synthesis of 1,3-thiazole-2-benzylidene amino cholesteryl carbonate derivatives **(7a-c/8)** (Final Schiff's base derivatives)*

In 20 ml of methanol/chloroform (v: v=1:1), a mixture of compound **(3a-c/5)** (0.002 mol) and 2-amino-1,3-thiazole **(6)** (0.002 mol) was refluxed for 10-12 h. Few drops of glac. HAc was used as catalyst. The reaction's progress was monitored by TLC. The reaction mixture was left overnight, resulting in a pale yellow-green product. The product thus obtained was filtered and subsequently recrystallized from a mixture of chloroform and methanol until consistent transition temperatures were achieved, resulting in the formation of pale greenish-yellow crystals.

Compound 7a: Pale yellow crystalline solid, yield 78%; IR (KBr, ν_{max}, cm^{-1}): 3035, 2948, 2896, 2847, 1754, 1623, 1605, 1506, 838; ^{1}H-NMR ($CDCl_3$, 400 MHz): δ (ppm) = 9.08 (s, 1H, -CH=N-), 8.01 (d, 1H, J = 3.6 Hz, C_4-thiazole), 7.67 (d, 2H, J = 8.6 Hz, Ar-H), 7.33 (d, 1H, J = 4 Hz, C_5-thiazole), 7.26 (d, 2H, J = 8.8 Hz, Ar-H), 5.42 (m, 1H, -C=CH-), 4.60 (m, 1H, -OC<u>H</u>-CH_2-), 2.49 (q, 2H, -OCH-C<u>H</u>$_2$-), 2.03-0.68 (m, 47H, -CH, -CH_2 and -CH_3); ^{13}C NMR ($CDCl_3$, 400MHz): δ(ppm) = 171.80, 160.02 (-CH=N-), 153.62, 150.00 (-O-COO-), 143.56, 139.82, 132.58, 121.77, 121.68, 118.48, 79.48, 56.14, 49.99, 39.71, 37.91, 36.81, 35.79, 31.91, 31.84, 28.02, 27.61, 24.28, 23.82, 22.82, 22.20, 21.05, 19.28, 18.71; Elemental analysis: calculated for $C_{41}H_{58}N_2O_3S$ (%): C, 74.73; H, 8.87; N, 4.25: found: C, 74.66; H, 8.79; N, 4.20.

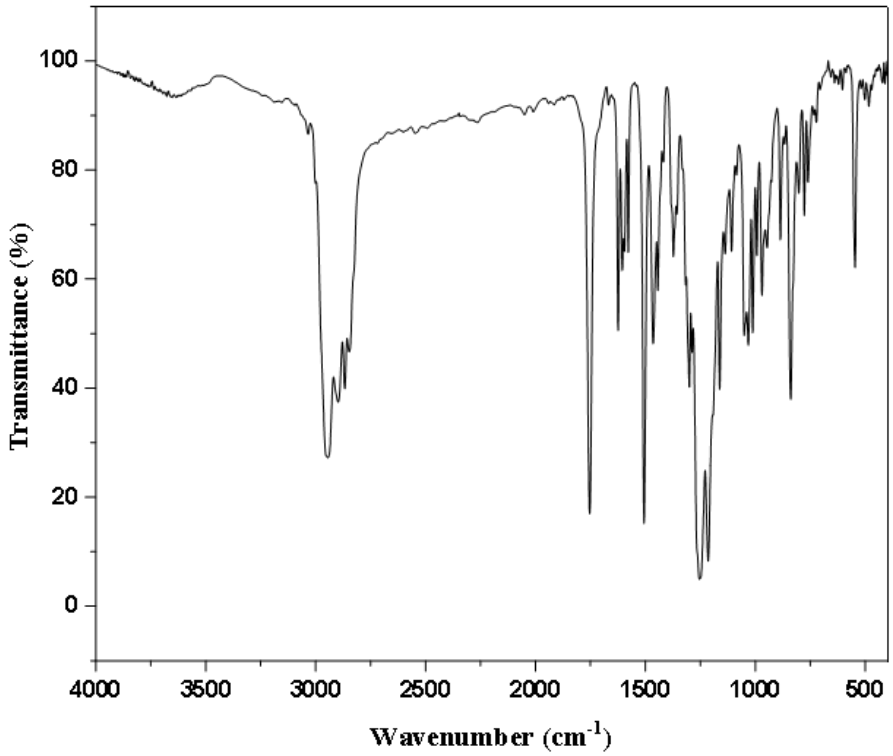

Figure 6.3 (a): IR Spectra of compound **7a**

Compound 7b: Pale yellow crystalline solid, yield 74%; IR (KBr, ν $_{max}$, cm^{-1}):3037, 2949, 2868, 2850, 1757, 1626, 1508, 844; ^{1}H-NMR ($CDCl_3$, 400 MHz): δ (ppm) = 9.00 (s, 1H, -CH=N-), 7.87 (d, 1H, J = 2.8 Hz, C_4-thiazole), 7.65 (s, 1H, Ar-H), 7.48 (d, 1H, J = 3.6 Hz, C_5-thiazole), 7.21 (d, 1H, J = 8.7 Hz, Ar-H), 7.01 (d, 1H, J = 8.8 Hz, Ar-H), 5.42 (m, 1H, -C=CH-), 4.60 (m, 1H, -OC<u>H</u>-CH_2-),3.87 (s, 3H, -OCH_3), 2.48 (q, 2H, -OCH-C<u>H_2</u>-), 2.03-0.68 (m, 47H, -CH, -CH_2 and -CH_3); ^{13}C NMR ($CDCl_3$, 400MHz): δ(ppm) = 171.80, 160.06 (-CH=N-), 151.71, 150.04 (-O-COO-), 140.01, 139.79, 123.43, 121.77, 120.83, 111.10, 79.46, 56.69, 56.14, 52.63, 49.99, 42.32, 39.71, 39.52, 37.93, 36.83, 36.56, 36.18, 35.79, 31.91, 31.84, 28.22, 28.02, 27.63, 24.28, 23.82, 22.82, 22.56, 21.05, 19.38, 18.77, 11.89; Elemental analysis: calculated for $C_{42}H_{60}N_2O_4S$ (%): C, 73.22; H, 8.78; N, 4.07: found: C, 73.12; H, 8.67; N, 3.91.

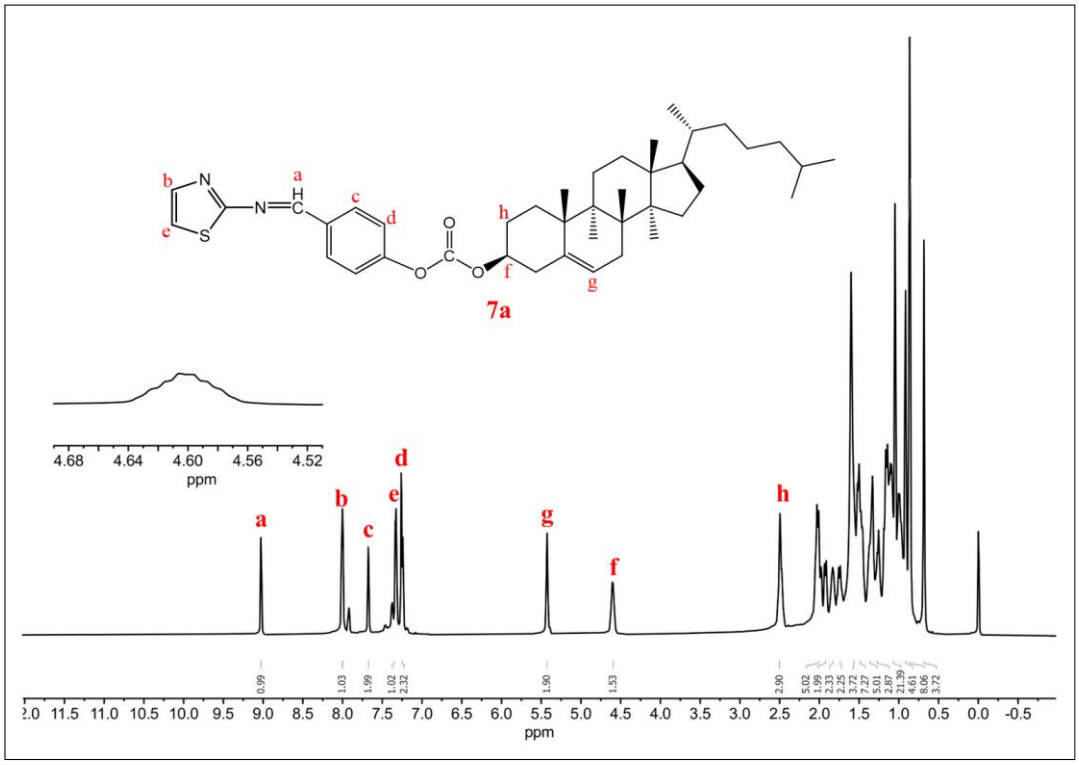

Figure 6.3 (b): ^{1}H-NMR spectra of compound **7a**

Compound 7c: Pale yellow crystalline solid, yield 83%; IR (KBr, ν $_{max}$, cm^{-1}):3036, 2951, 2868, 2852, 1757, 1624, 1508, 842; ^{1}H-NMR ($CDCl_3$, 400 MHz): δ (ppm) = 8.95 (s, 1H, -CH=N-), 7.72 (d, 1H, J = 3.2 Hz, C_4-thiazole), 7.67 (s, 1H, Ar-H), 7.41 (d, 1H, J = 3.6 Hz, C_5-thiazole), 7.40 (d, 1H, J = 8.8 Hz, Ar-H), 7.22 (d, 1H, J = 8.6 Hz, Ar-H), 5.42 (m, 1H, -C=CH-), 4.60 (m, 1H, -OC<u>H</u>-CH_2-), 4.18 (q, 2H, -OC<u>H_2</u>-CH_3), 2.48 (q, 2H, -OCH-C<u>H_2</u>-), 2.03-0.68 (m, 50H, -CH, -CH_2 and -CH_3); ^{13}C NMR ($CDCl_3$, 400MHz): δ(ppm) = 172.89, 162.36 (-CH=N-), 152.06, 151.39 (-O-COO-), 144.05, 141.47, 139.18, 133.86, 124.44, 123.22, 122.62, 118.27, 111.81, 79.18, 64.69, 56.69, 56.14, 49.99, 42.32, 39.72, 39.52, 37.88, 36,83, 36.57,

36.19, 35.79, 31.91, 31.85, 28.13, 28.02, 27.56, 24.29, 23.83, 22.83, 22,57, 21.06, 19.30, 18.72, 14.70, 14.63, 11.87; Elemental analysis: calculated for $C_{43}H_{62}N_2O_4S$ (%): C, 73.46; H, 8.89; N, 3.98: found: C, 73.28; H, 8.74; N, 3.82.

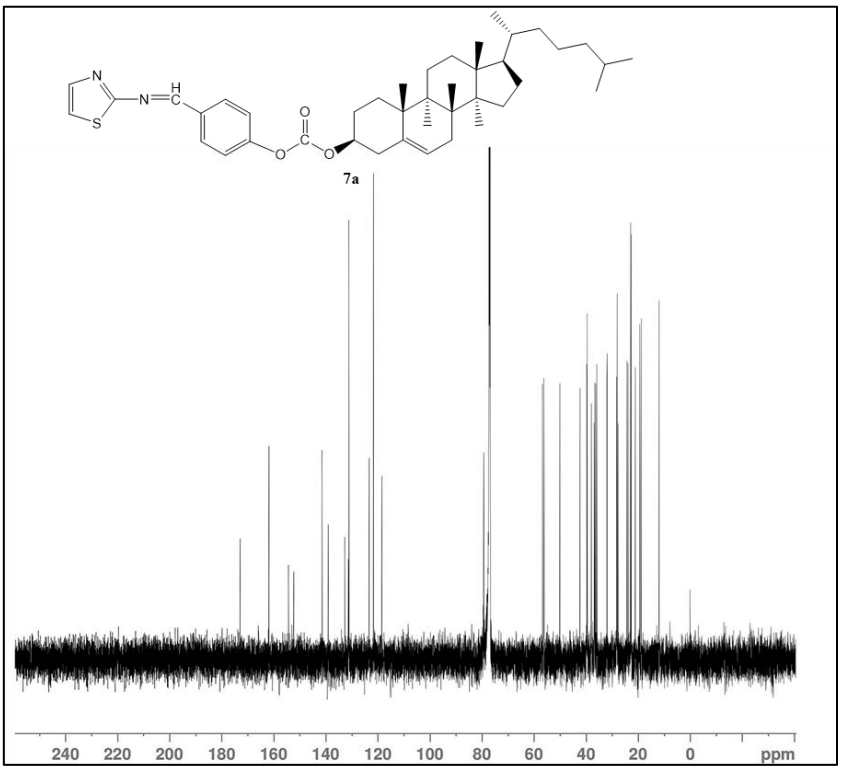

Figure 6.3 (c): ^{13}C-NMR spectra of compound **7a**

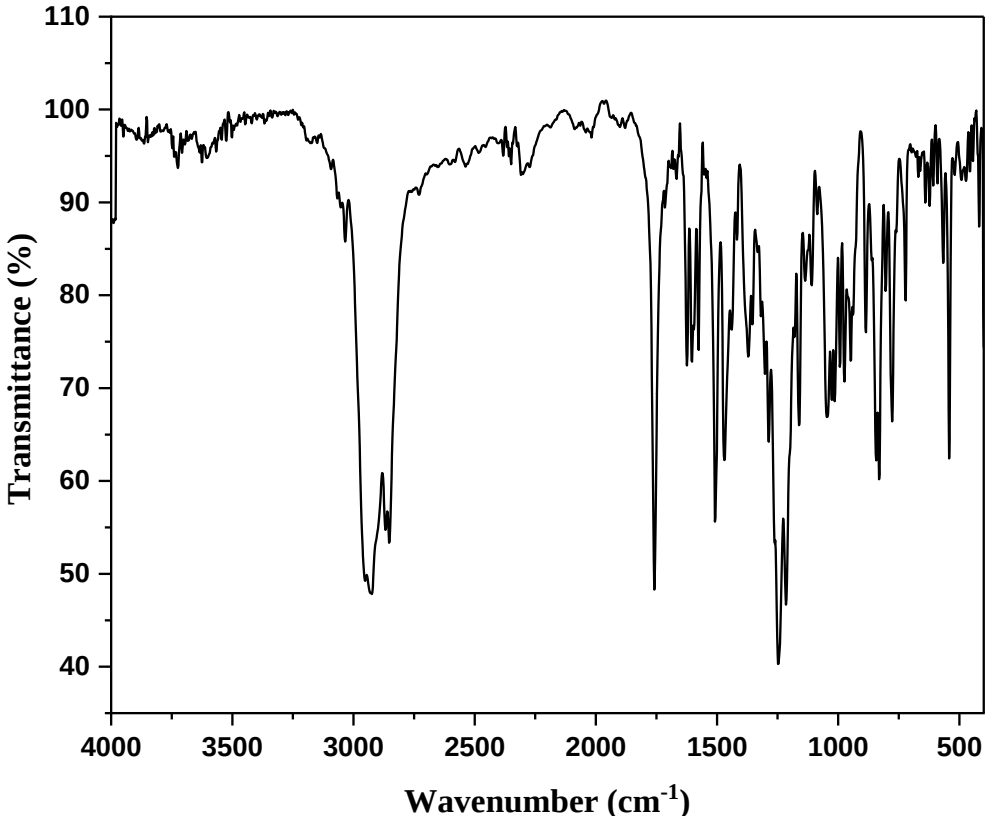

Figure 6.4 (a): IR Spectra of compound **8**

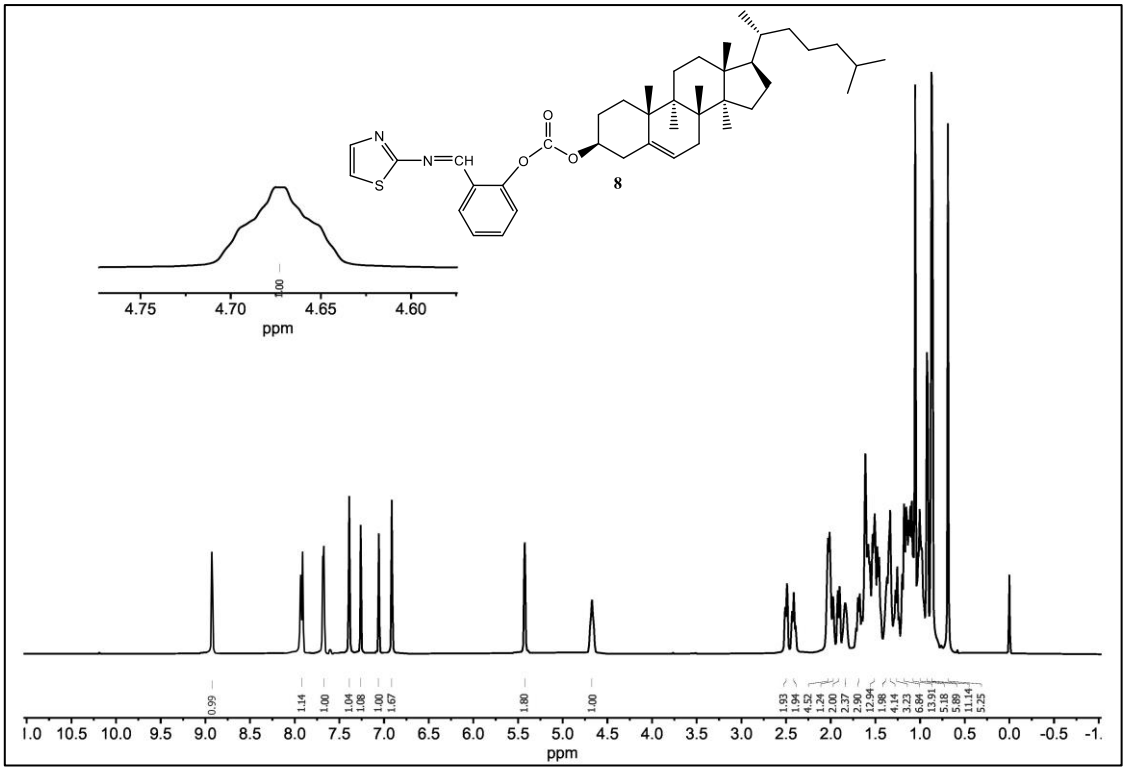

Figure 6.4 (b): ^{1}H-NMR spectra of compound **8**

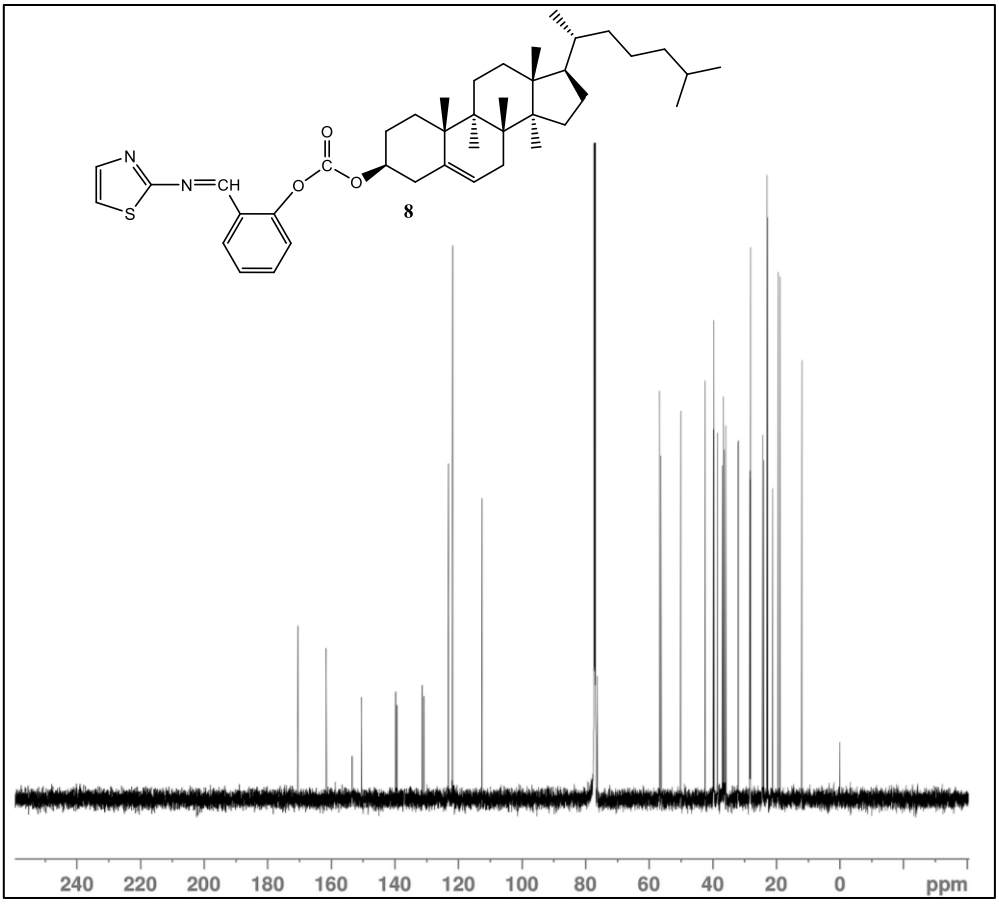

Figure 6.4 (c): ^{13}C-NMR spectra of compound **8**

Compound 8: Pale yellow crystalline solid, yield 80%; IR (KBr, ν_{max}, cm^{-1}): 3036, 2953, 2868, 2852, 1759, 1624, 1508, 842; ^{1}H-NMR ($CDCl_3$, 400 MHz): δ (ppm) = 8.99 (s, 1H, -CH=N-), 7.89 (d, 1H, J = 0.8 Hz, C_4-thiazole), 7.67 (d, 1H, J = 22 Hz, Ar-H), 7.42 (d, 1H, J = 1.6 Hz, C_5-thiazole), 7.33 (d, 1H, J = 18 Hz, Ar-H), 7.19 (d, 1H, J = 20 Hz, Ar-H), 6.88 (d,1H, J = 20 Hz , Ar-H) 5.42 (m, 1H, -C=CH-), 4.60 (m, 1H, -OC<u>H</u>-CH_2-), 4.18 (q, 2H, -OC<u>H_2</u>-CH_3), 2.48 (q, 2H, -OCH-C<u>H_2</u>-), 2.03-0.68 (m, 50H, -CH, -CH_2 and -CH_3); ^{13}C NMR ($CDCl_3$, 400MHz): δ(ppm) = 171.58, 160.01 (-CH=N-), 154.08, 150.40 (-O-COO-), 140.80, 139.18, 134.10, 131.12, 123.12, 121.24, 112.51, 76.26, 56.69, 56.15, 50.00, 42.33, 39.72, 39.52, 38.40, 36.92, 36.58, 36.18, 35.80, 31.86, 28.11, 28.02, 24.28, 23.84, 22.82, 22.56, 21.05, 19.36, 18.71, 11.87. Elemental analysis: calculated for $C_{41}H_{58}N_2O_3S$ (%): C, 74.73; H, 8.87; N, 4.25: found: C, 74.59; H, 8.74; N, 4.13.

6.2.4. General procedure for in vitro anti-microbial evaluation

In vitro anti-microbial activities were studied with the well diffusion method. The samples were dissolved in DMF. For the antibacterial and antifungal assay, positive controls used were amoxicillin and ketoconazole solutions, respectively. Both experiments used DMF solvent as a negative control. After incubation, inhibition zones were measured to determine activity.

The stock solution of agar media was made by dissolving 30 gm agar and 13.6 gm nutrition broth in 1000 ml sterile water. Agar medium was placed into sterilized petri plates to solidify. After solidification, 100 µl of bacterial culture was evenly distributed on the agar surface for the antibacterial investigation, and 100 µl of fungal inoculum was spread for the antifungal study, using a spreader until the inoculum dried. Subsequently, sterile cork borers were used to create wells in the petri dishes containing the respective inoculums.

Next, 100 µl of each sample, as well as the positive and negative control solutions, were added to separate wells in the petri dishes. The positive control (Amoxicillin/Ketoconazole) was used to verify the experimental setup's ability to detect antibacterial and antifungal activity, given its well-established effects. The negative control (DMF) was used to confirm that any observed activity was specific to the samples being tested and not a result of the solvent.

The petri dishes were incubated at 37°C for 18-24 hrs for the antibacterial study and 48-72 hours for the antifungal study. After the incubation period, the antibacterial and antifungal activity were evaluated by measuring the diameter of the inhibitory zone around each well. Larger inhibition zones indicated stronger antibacterial or antifungal activity against

the tested microorganisms. By performing these experiments, the potential antibacterial and antifungal properties of the samples were evaluated.

6.2.5. General procedure for anti-oxidant assay

The synthesized compounds were tested for their in vitro antioxidant properties using the method provided in literature. [22]. In short, 0.01 mg/mL (0.001% (w/v)) DPPH solution using methanol as solvent was prepared. Drug stock solution (1 mg/mL) was made upto the final concentrations of 25, 50, 100, 150 and 200 µg/mL using DMSO solvent. The control consists of 1 mL of DPPH solution diluted with 4 mL of DMSO. Absorbance was measured against blank at λ_{max} of 517 nm using UV–Visible Spectrophotometer (Shimadzu UV-1800 spectrophotometer- Japan) [23]. The % inhibition against DPPH for all the compounds were calculated using [24].

$$\text{“\% Inhibition} = [(A_{control} - A_{sample}) / A_{control}] \times 100\text{”}$$

where $A_{control}$ = abs. of control, A_{sample} = abs. of test compounds.

6.2.6. Computational methods

The compounds' 2D structures were drawn on online platform of Molinspiration (https://www.molinspiration.com/cgi-bin/properties) and the physiochemical parameters were determined for each structure separately.

DFT study were conducted using the Gaussian 09, release A.02 software program [25], B3LYP method and 6-31G (d, p) basis set were used for geometry optimization. The “frontier molecular orbitals analysis” (FMOs) and “molecular electrostatic potential” (MEP) surfaces for compounds **7a-c** and **8** were calculated at the same level of theory and visualized with the graphical interface Gauss View 05 (Gaussian Inc., Wallingford, CT, USA). Various chemical reactivity descriptors were also calculated [26,27].

6.3. Results and discussion

6.3.1. Chemistry

The synthetic approach for the synthesis of all thiazole derivatives **(7a-c** and **8)** (Final Schiff’s base derivatives) is depicted in Scheme 6.1. The cholesteryl chloroformate **(2)** was employed as the precursor material in an efficient synthesis of all the compounds. The essential intermediates, substituted formyl phenyl cholesteryl carbonates **(3a-c** and **5)**, were synthesised by a one-step procedure that involves reacting cholesteryl chloroformates with different

substituted hydroxy benzaldehyde **(1a-c** and **4)** in presence of anhydrous pyridine as proton scavenger in good yields.

Finally, the target compounds **(7a-c** and **8)** were obtained in good yields (75-80%) by simple condensation of 2-amino-1,3-thiazole **(6)** with equimolar quantities of four different substituted formyl phenyl cholesteryl carbonates.

All the newly synthesized 1,3-thiazole-2-benzylideneamino cholesteryl carbonate derivatives **(7a-c** and **8)** were characterized using elemental analysis and spectral techniques such as FT-IR, ^{1}H-NMR and ^{13}C-NMR analysis. In FT-IR, the aldehyde derivative 4-formyl phenyl cholesteryl carbonate **(3a)** displayed exhibited obvious bands (ν_{max}, cm^{-1}) at 2942, 2878, 2862, 2850 ν (-CH aliphatic), 2721 (-CH stretch -CHO group),1756 (-C=O of carbonate), 1704 (-CH stretch -CHO group), 1450-1500 (-CH ar.), 1576 cm^{-1} (-C-C ar.) stretch. **(7a)** displays prominent IR bands at 2945, 2846 (-CH aliphatic), 1754 (-C=O carbonate), and 1626 cm^{-1} (-CH=N- imine) after condensation with 2-amino-1,3-thiazole **(6)**. The disappearance of bands at 1704 and 2721 cm^{-1} of aldehyde group (-CHO) and the emergence of peak at 1626 cm^{-1} due to azomethine group (-CH=N-) indicates condensation to form final Schiff base, thereby confirming structure of 1,3-thiazole-2-benzylideneamino-4'-cholesterylcarbonate **(7a)**.

The ^{1}H NMR of **(3a)** displayed an evident signal at δ 9.91 ppm due to aldehyde group (s, 1H, -CHO). The proton NMR of the final Schiff's base 1,3-thiazole-2-benzylideneamino-4'-cholesteryl carbonate **(7a)** depicts signals at δ9.02 (s, 1H, -CH=N-), δ 8.01-7.26 (m, 6H, Ar-H and H-thiazole), δ 5.42 (d, 1H, olefinic H in cholesterol), δ 4.64 (m, 1H, H of cholesterol near carbonate linkage), δ 2.49 (d, 2H, -OCH-C$\underline{H}_2$), δ 2.05-0.70 (m, 41H, -CH,-CH_2 and -CH_3 of cholesterol) ppm, respectively. The presence of an imine linkage-induced signal at 9.02 ppm and the dissipation of the singlet at 9.91 ppm indicate that 1,3-thiazole-2-benzylideneamino-4'-cholesteryl carbonate has been formed **(7a)**. The ^{13}C NMR spectra of **(3a)** exhibit significant peaks at δ 191.2 of aldehyde group (-CHO) and δ 150.1 carbonyl (-O-COO-) ppm, whereas **(7a)** displays signal at δ 173.5 (C_2-thiazole), δ 162.5 (azomethine -CH=N-), δ 152.56 (carbonyl carbon -O-COO-), and δ 131.29-118.48 (C from ar. rings) ppm. The presence of the imine carbon (-CH=N-) at a chemical shift of δ162.5 ppm indicates the synthesis of final compound **(7a)**.

The rest of the series members **(7a-c** and **8)** show almost identical IR, NMR (^{1}H and ^{13}C) bands and are included in the synthesis.

6.3.2. In-vitro anti-microbial evaluation

All of the compounds were tested for in-vitro antibacterial and antifungal activity. The investigated compounds were in-vitro evaluated for antibacterial activity against *S Aureus*, *E Coli*, and *A Niger* and *C Albicans*. Standard control drugs for antibacterial and antifungal assays included amoxicillin and ketoconazole. **Table 6.1** and **Table 6.2** shows antibacterial and antifungal zone of inhibition (mm) and % activity index data respectively.

Results indicated that all the synthesized derivatives show significant antibacterial activity as shown in **Figure 6.5** against both bacterial strains when compared with standard amoxycillin **(Table 6.1)**. Compound **7a** and **8** were most potent towards the *S. aureus* with percentage activity index of 90% and 87.5% respectively, compared to standard. Against E. coli, compounds **7a**, **7c**, and **8** showed high bacteriostatic activity, surpassing the control drug with percentage activity index of 105 %, 100% and 104.58 % respectively. The synthesized compounds were less active against Gram-positive rather than Gram-negative bacteria.

Table 6.1: Anti-bacterial assay of compounds **7a-c** and **8**[a]

Compound code	***S. aureus***		***E. coli***	
	Gram positive bacteria		**Gram negative bacteria**	
	Zone (mm)	**% activity**	**Zone (mm)**	**% activity**
7a	18	90	25.5	106.25
7b	15.5	77.5	22	91.67
7c	16	80	24	100
8	17.5	87.5	25	104.17
Amoxycillin (STD)	20	100	24	100
Control [b]	-	-	-	-

[a] Concentration for all the compounds as well as amoxycillin (STD) was 200µg/ml

[b] Control - DMF; No inhibition

The antifungal evaluation results presented in **Table 6.2** showed that derivatives **7a**, **7c**, and **8** demonstrated moderate activity against *A. Niger*, with percentage activity indexes of 94.45%, 72.22%, and 77.78%, respectively, compared to the reference drug ketoconazole. Additionally, compounds **7a** and **8** exhibited noteworthy activity against *C. albicans*, surpassing effectiveness of the control drug **(Figure 6.5)**.

Table 6.2: Anti-fungal assay of compounds **7a-c** and **8**[a]

Compound code	*Aspergillus niger*		*Candida albicans*	
	Zone (mm)	% activity	Zone (mm)	% activity
7a	17.5	97.22	22.5	107.14
7b	8	44.45	12	57.14
7c	13.5	75	10	47.61
8	14	77.78	24.5	116.67
Ketoconazole (STD)	18	100	21	100
Control [b]	-	-	-	-

[a] Concentration for all the compounds as well as amoxycillin (STD) was 200µg/ml

[b] Control - DMF; No inhibition

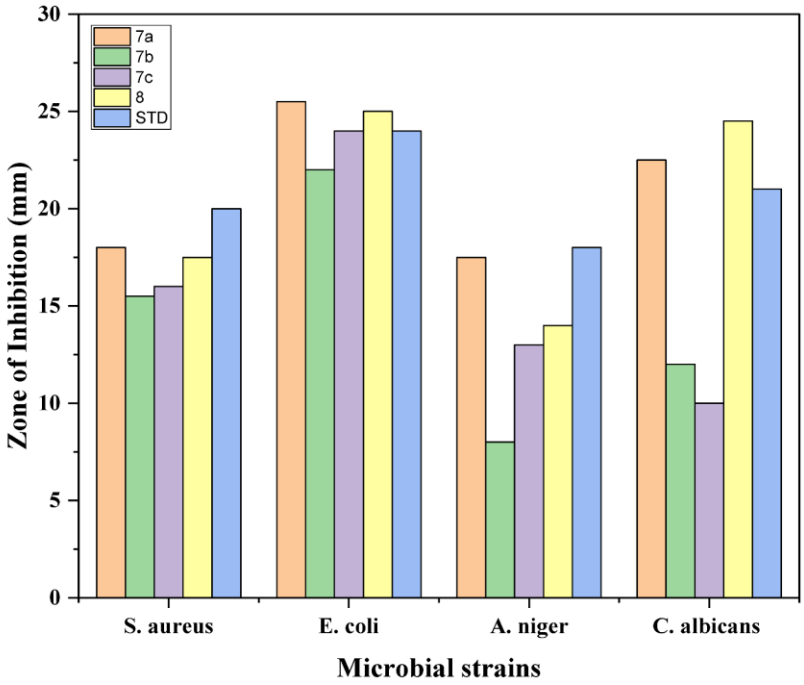

Figure 6.5: Graphical representation of zone of inhibition for compounds **7a-c** and **8** against different microbial stains

The compounds' strong antibacterial action is likely due to their large dipole moment, which is brought by the Schiff's base linkage in the molecules [28,29]. This dipole moment contributes to improved interactions with microbial cells, potentially leading to higher antimicrobial agent efficiency. The electron-donating methoxy and ethoxy substituents in the core ring reduce the reactivity of compounds **7b** and **7c** by increasing the electron density of the molecule, potentially decreasing the overall electrophilicity of the compound.

Antimicrobial activity is often related with the ability to interact with specific nucleophilic centres in microbial cells. A decrease in electrophilicity may hinder these interactions.

6.3.3. In vitro anti-oxidant assay

DPPH assay was used to measure radical scavenging activity of synthesized compounds. The percentage of inhibition and IC_{50} indicate antioxidant activity. It was compared to ascorbic acid.

Table 6.3 shows that all synthesised derivatives showed comparable radical scavenging activity, with **7c** having the lowest activity at 200 µg/mL (57.97±0.15%). The IC_{50} value of 138.73 µg/mL was also the lowest for this compound. Compounds **7a** and **8** showed superior scavenging activity, with IC_{50} values of 108.08 and 101.32 µg/mL. Notably, the antioxidant efficacy of compounds **7b** and **7c** is adversely affected by the addition of electron-donating groups to the phenyl ring in the lateral position.

Overall, the compounds exhibited lower potency compared to the reference compound. Compounds **7a** and **8** demonstrated a slightly superior antioxidant activity compared to the other synthesized compounds, as illustrated in **Figure 6.6**.

Table 6.3: Antioxidant activity: % inhibition and IC_{50} values of compounds **7a-c** and **8**

Sample	**% Inhibition**[a] (at different µg/mL)						**IC_{50}**
	0	**25**	**50**	**100**	**150**	**200**	**(µg/mL)**
7a	0	36.08±0.10	48.07±0.40	58.02±0.11	58.54±0.20	66.71±0.27	108.08
7b	0	29.17±0.37	39.48±0.25	41.98±0.06	56.81±0.15	63.40±0.62	130.81
7c	0	27.65±0.20	31.82±0.16	48.08±0.17	55.24±0.09	57.97±0.15	138.73
8	0	39.16±0.15	47.01±0.27	51.76±0.20	66.08±0.19	71.84±0.43	101.32
STD[b]	0	45.17±0.15	61.26±0.15	77.52±0.06	88.55±0.08	97.36±0.10	59.48
Control[c]	-	-	-	-	-	-	-

[a] Values represent the mean ± standard error mean (SEM) of three experiments.

[b] Ascorbic acid used as standard

[c] No inhibition

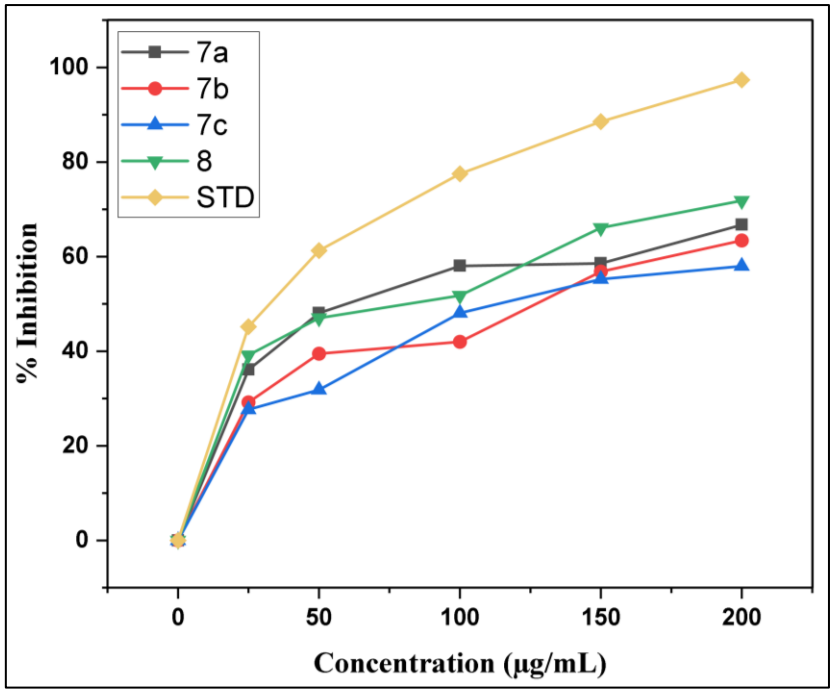

Figure 6.6: Graphical representation of DPPH radical scavenging activities of compounds **7a-c** and **8**

6.3.4. Texture analysis / Liquid crystal properties

Liquid crystals exhibit properties of both solid crystals and conventional liquids. They frequently appear in the temperature range that exists between the crystal and isotropic liquid phase and are defined by having properties that are anisotropic without a 3-D crystal structure [30]. Although the molecules of liquid crystals can be arranged to resemble crystals, they can still flow like liquids.

Researchers are interested in cholesterol-based liquid crystals because of its natural and commercial availability, as well as their distinctive optical properties. LC based on cholesterols shows circular dichroism, selective reflection, electrooptic effects and specific rotations, due to their helical super structure. Researchers are interested in these properties [31].

Polarizing optical microscopes were used to study the LC properties of all synthesised compounds in heating as well as cooling cycles at 5 °C per minute. From all the synthesized compounds only compound **7a** possesses mesomorphic property showing enantiotropic chiral nematic (N*) phase. It showed vibrant colours in the N* phase at different temperatures, possibly due to helical pitch unwinding [32].

As observed, compound **7a** shows the textures resembling oily streaks of cholesteric **Figure 6.7 (a)** mesophase at 210.6 °C and clears at 229.7 °C. When transitioning from the isotropic phase to a lower temperature at 213.7 °C, the droplet-shaped nematic texture

reappeared, gradually combined, and transformed into the nematic schlieren texture **Figure 6.7 (b)**, that appears like the Smectic A phase that turns into Grandjean planar upon shearing under crossed polarizers prior to crystallization at 100.9 °C.

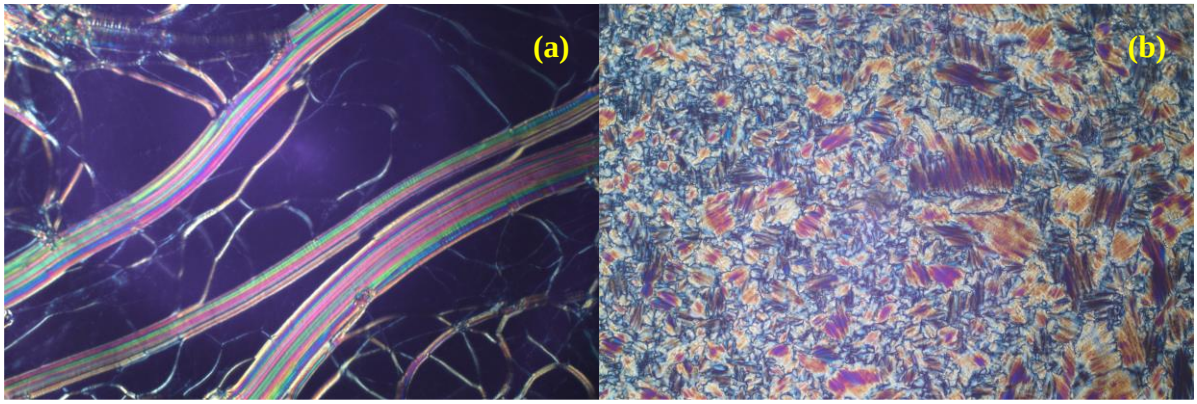

Figure 6.7: Microphotographs of the optical textures **(a)** oily streaks texture of cholesteric phase/chiral nematic (N*) of **7a** on heating at 210.6 °C, **(b)** nematic schlieren texture (N*) of **7a** on cooling at 213.7 °C

The other derivatives of the series namely **7b**,**7c** and **8** are non-mesogenic in character. In the compound **7b** and **7c** lateral substitution of the central core with bulky methoxy(-OCH_3) and ethoxy(-OC_2H_5) groups plays important role in destroying the mesomorphic character by disrupting the alignment of the molecule [33,34]. Also, the lateral substitution shields the substituent from the rest of the molecule, which may decrease mesogenic character [35]. Ahmed et.al., suggests that a lateral substituent in a nematogenic molecule can decrease thermal stability LC phase due to steric hindrance [36]. Every lateral substitution increases the molecules breadth, resulting in decreased "length-to-breadth" ratio, according to molecular statistical theory, which generally lowered clearing temperatures as observed in the compounds **7a-c** [37]. The non-mesomorphic character of the compound **8** can be ascribed to steric hindrance of the molecule and also its shape which resembles a bent rod unlike the compound **7a** which has a rod like shape [38].

6.3.5. Thermal properties

The mesophase observed under the polarising optical microscope was further confirmed by DSC. **Table 6.4** shows mesomorphic transition temperatures and related ΔH values (indicated in parentheses) for the mesogen **7a**. Representative DSC thermograms for the synthesised compound **7a** is presented in **Figure 6.8**.

The DSC thermograms of the derivative **7a** exhibited an enantiotropic mesophase transition. Compound **7a** shows sharp exothermic peak at 210.12°C (ΔH = 16.1 kJ/mol) corresponding to the Cr-N* phase transition and shows cholesteric to isotropic at 228.70°C (ΔH = 1.38 kJ/mol) in the heating scan. In the cooling scan the peak at 213.71°C (ΔH = 1.04 kJ/mol) corresponds to the N* mesophase till the crystallization at 98.86°C (15.7 kJ/mol). As observed, the enthalpy change (ΔH) is minimum in the nematic-to-isotropic transition because the molecules are already partially disordered in the nematic phase and do not need to break strong intermolecular forces as in the crystal-to-nematic transition.

Table 6.4: Phase-transition temperature in °C and enthalpy changes [kJ mol^{-1}] data for compounds **7a-c** and **8**

Compound	Phase[a] transition temperature (°C)[b] and Enthalpy change [kJ mol^{-1}][c]
7a	Cr 210.1 [16.1] N* 228.7 [1.38] I 213.7 [1.04] N* 98.8 [15.7] Cr
7b	Cr 209.5 I
7c	Cr 165.7 I
8	Cr 296.3 I

[a] Cr : Crystal, N* : cholesteric mesophase, I : Isotropic

[b] Obtained/confirmed using POM as well as DSC

[c] Obtained from DSC

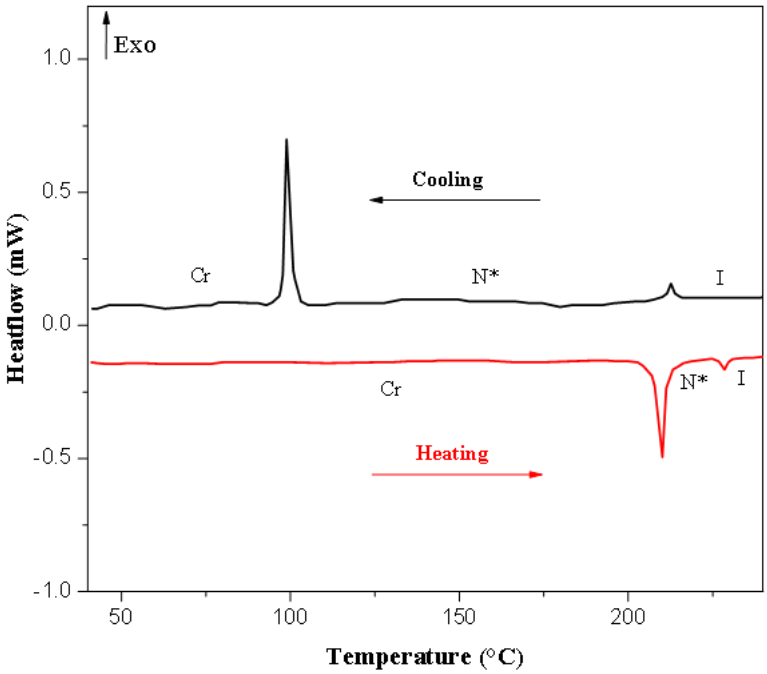

Figure 6.8: DSC thermogram of compound **7a**

TGA was used to assess the thermal stability of all the synthesised derivatives. This was crucial particularly for **7a** which shows mesomorphic transitions. This was particularly essential for **7a**, which displays phase transitions. The thermogram of **7a** shows decomposition starting at approximately 264 °C, with 74% of the compound decomposing close to 351 °C. The mesogen **7a** was found to be stable at N*-I transition temperatures. The compound exhibits LC property prior to undergoing thermal decomposition. Additionally, TGA results indicate that the framework of **7b, 7c** and **8** are stable up to 264 °C, 223 °C and 363 °C respectively **Figure 6.9**. The superior thermal stability of the **8** is due to the core ortho substitution which can lead to steric hindrance. Because the substituents are so close together, they might establish repulsive interactions, making it energetically unfavourable for the molecule to adopt certain conformations. As a result, the rotational freedom around the C-C single bonds is reduced, resulting in a greater energy barrier for thermal rearrangement or isomerization reactions. Therefore, **8** exhibits greater thermal stability due to its reduced susceptibility to undergo structural modifications.

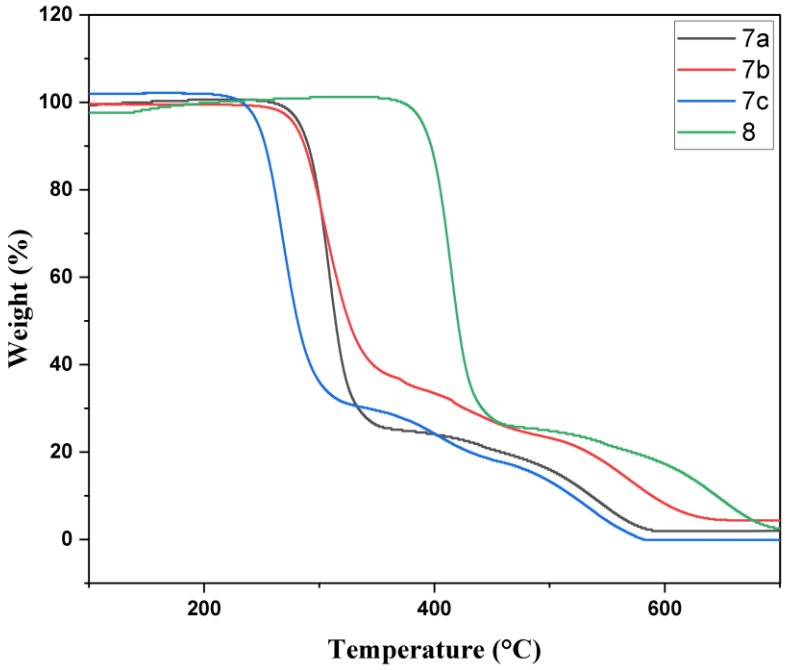

Figure 6.9: TGA thermogram of compounds **7a-c** and **8**

6.3.6. Optical properties

The UV-visible spectra of **7a-c** and **8** recorded in chloroform and are given in **Figure 6.10** with relevant photo-physical data displayed in **Table 6.5**. The absorption spectra's of **7a-c** were all relatively comparable due to their structural similarities except compound **8** which has ortho substitution. The λ_{max} of **7a-c** were approximately near to 334-338 nm. These were

also the maximum absorption peaks for **7a-c**. The peak around 270 nm is caused by the π- π* transition of the aromatic ring [39], and the peak around 337 nm is caused by n- π* transition of the azomethine (CH=N) group, involving the π-electron system of the entire mesogenic moiety, with considerable charge transfer characteristic [40]. Compound **7b** and **7c** exhibit a little red shift in comparison to **7a**. This may be due to the changes in the electronic structure due to methoxy and ethoxy group substitution, which in turn affect the delocalization of electrons within the molecule, causing a bathochromic shift in absorption spectrum.

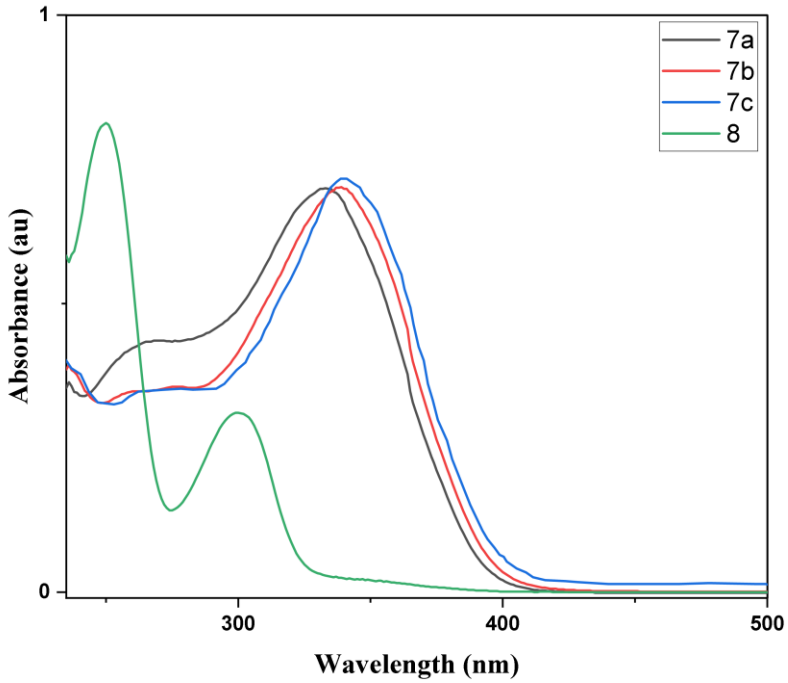

Figure 6.10: UV-vis spectra of compounds **7a-c** and **8**

The reduction of UV absorbance shift of **8** as compared to **7a-c** is primarily due to the influence of steric hindrance and the resulting impact on the electronic distribution within the molecule. In compound **8**, the substituents are positioned on adjacent carbon atoms of the aromatic ring, leading to steric hindrance, which can affect the arrangement of the substituents and the electronic structure of the molecule. The steric hindrance in **8** can disrupt the conjugation and electronic distribution within the molecule, reducing the extent of delocalization of π-electrons. This reduction in π-electron delocalization weakens the electronic transitions responsible for UV absorbance and leads to a smaller shift in the absorption wavelength compared to **7a-c**.

Photoluminescence (PL) plays an important role in liquid crystalline materials [41,42], biochemical and biomedical research [43], molecular biology and genetics [44], medical diagnostics [45], material sciences and nanotechnology [46], optics and photonics [47,48], etc. The PL spectra of compounds were carried out in $CHCl_3$ ($1x10^{-5}$ M) at wavelengths 300-700

nm and an excitation wavelength set to 340 nm for compounds **7a-c** and 300 nm for compound **8** to explore the relationship between their structures and spectral properties. The emission as well as excitation bandwidths for all studies were fixed at 5 nm. The PL spectra of **7b,7c** and **8** are all similar in nature. However, for compounds **7a,** the curve is of a distinct pattern and the maxima shifted to a lower wavelength. As seen in the spectra **Figure 6.11** the derivatives **7b** and **7c** shows enhanced PL intensity, this may be due to the electron donating group substituted laterally to the core ring. Electron donating groups tend to promote more efficient fluorescence emission. Comprehensive photophysical data are displayed in **Table 6.5**.

Table 6.5: UV and PL spectral data for compounds **7a-c** and **8**

Compound	UV(nm)	Fluorescence(nm)	Stokes shift(nm)	Φ_{PL}[a]
7a	268, 334	412	78	0.11
7b	261, 339	396,430,456	57	0.23
7c	264, 341	415,433,463	74	0.22
8	250, 300	412,434,461	112	0.14

[a]Determined with quinine sulphate as STD (Φ_{PL} = 0.546 in 1 N H_2SO_4)

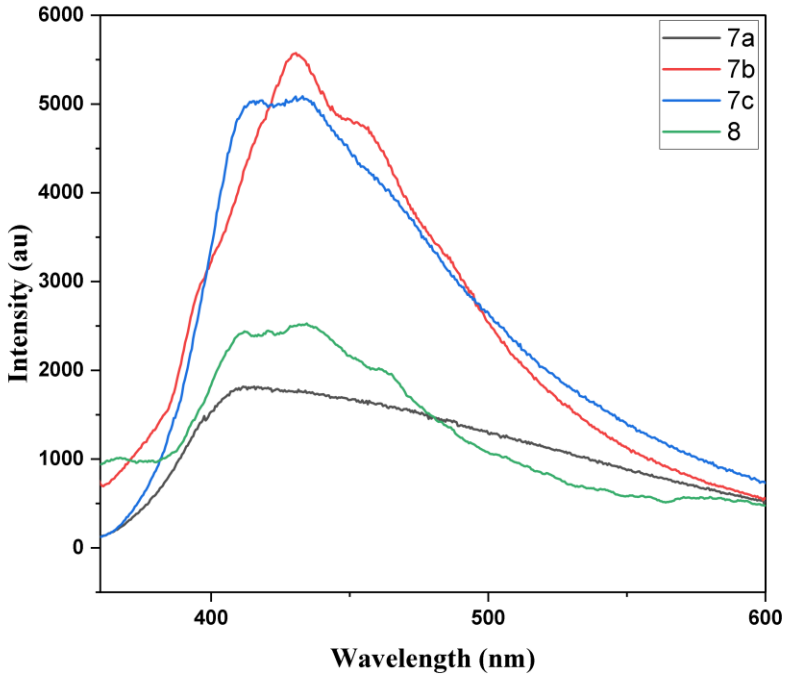

Figure 6.11: PL spectra of compounds **7a-c** and **8**

The examination of fluorescence quantum yields in $CHCl_3$ (1×10^{-6} M) solution shows that all the compounds show photoluminescence quantum yield ranging between 0.11 to 0.23 when in comparison to the reference (quinine sulphate in 1 N sulfuric acid; Φ_{PL} = 0.546). This

highlights their unique molecular behavior and suggests their considerable promise in optoelectronics and photonics applications. Compounds **7a** and **7b** exhibits a more intense emission, leading to an increased PL quantum yield. The stokes shifts displayed by all compounds are given in **Table 6.5**.

The photoluminescence spectra of all the synthesised compounds exhibit emission in the blue region (420–500 nm), indicating that all of the materials have blue light emission characteristics that can be used in potential applications such as, biotags for biological sensing applications, OLED materials and fluorescent probes in biological applications [49,50].

6.3.7. Drug-likeness and bioactivity score/ADME analysis

Drug-likeness and molecular characteristics are essential ideas in drug design. Drug-likeness is a qualitative concept that describes how "druglike" a substance is in terms of aspects such as bioavailability [51]. The pharmacokinetic properties of the synthesized thiazole cholesteryl carbonate derivatives were assessed using “Lipinski’s Rule of Five” [52]. These qualities filter drugs likeness and reflect physicochemical features of compounds, including “absorption, distribution, metabolism, and excretion” [53]. This criterion is extensively used to filter drug-likeness of a molecule. Absorption % is computed using the method [54].

“% ABS = 109-0.345 × (TPSA)”

Table 6.6 contains calculated Lipinski parameter as well as %ABS of the synthesised compounds **(7a-c and 8)**.

Table 6.6: Physicochemical properties of compounds **7a-c** and **8**

Sample Code	Mw (g/mol)	miLogP	HBA	HBD	TPSA	N violations	Volume	% ABS
7a	602.88	9.14	5	0	60.8	2	588.11	88.024
7b	632.91	9	6	0	70.03	2	613.65	84.83965
7c	646.94	9.13	6	0	70.03	2	630.46	84.83965
8	602.88	9.12	5	0	60.8	2	588.11	88.024

As indicated in **Table 6.6**, all the synthesised compounds have a relatively low number of H bond donors but a significant number of acceptors. The TPSA values of studied compounds are below threshold (82 Å), suggesting that the compounds have good drug permeability in cellular plasma membranes. Compounds **7a** and **8** have the highest absorption (88.02%) because they have the least topological polar surface area. In general, all synthesised

compounds **7a-c** and **8** were found to violate the Lipinski rule of five. However, current drugs like doxorubicin and erythromycin that are used to treat a number diseases also fail these requirements [55,56].

The bioactivity scores for 7**a-c** & **8** were also determined for six criteria as shown in **Table 6.7**. A compound is active if its bioactivity score is above 0.00, moderately active if between -0.50 and 0.00, and inert if <-0.50 [57]. The result in **Table 6.7**, predicted good bioactivity score for all the synthesised compounds. Some of the compounds under investigation have high activity, while others show moderate activity. Expect compound **8**, all the other derivatives i.e., **7a-7c** scored -0.77, -1.02 and 1.15 for ion channel modulator, respectively, and thus were considered inactive. All the derivatives were inactive against kinase inhibitor. Also, derivatives **7b** and **7c** were considered inactive against nuclear receptor ligand. Nevertheless, the other data for all derivatives showed favourable to moderate activity, having score that ranged from -0.49 to -0.04.

Table 6.7: Bioactivity scores of compounds **7a-c** and **8**

Sample	GPCR ligand	Ion-Channel Modulator	Kinase inhibitor	Nuclear receptor ligand	Protease inhibitor	Enzyme inhibitor
7a	-0.28	-0.77	-0.73	-0.31	-0.21	0.04
7b	-0.41	-1.02	-0.89	-0.53	-0.3	-0.15
7c	-0.49	-1.15	-1.01	-0.63	-0.35	-0.27
8	-0.27	-0.48	-0.74	-0.31	-0.2	0.03

6.3.8. DFT calculations

6.3.8.1. Optimized Molecular Structures and HOMO-LUMO Energies

DFT analysis was performed to explore the molecular conformation, Frontier MOs, and electrostatic potential distribution of cholesterol derivatives **7a-c** and **8**. The Gaussian 09, revision A.02 software package [25] was employed, utilizing the B3LYP "(Becke3–Lee–Yang–Parr hybrid functional)" method with 6-31G (d, p) basis set for full geometry optimization. We employed the B3LYP functional paired with the 6-31G std basis set, which has demonstrated its effective application in larger organic compounds and H bond systems in previous studies [58,59]. Optimized structures of all the compounds are depicted using the ball and stick model (**Figure 6.12**). The spheres show atoms—oxygen red, nitrogen blue, hydrogen

white, sulphur yellow, and carbon as grey coloured. The sticks interconnecting atoms depict their bonding arrangement. The optimized energy minima for **7a-c** and **8** are shown in **Table 6.8**.

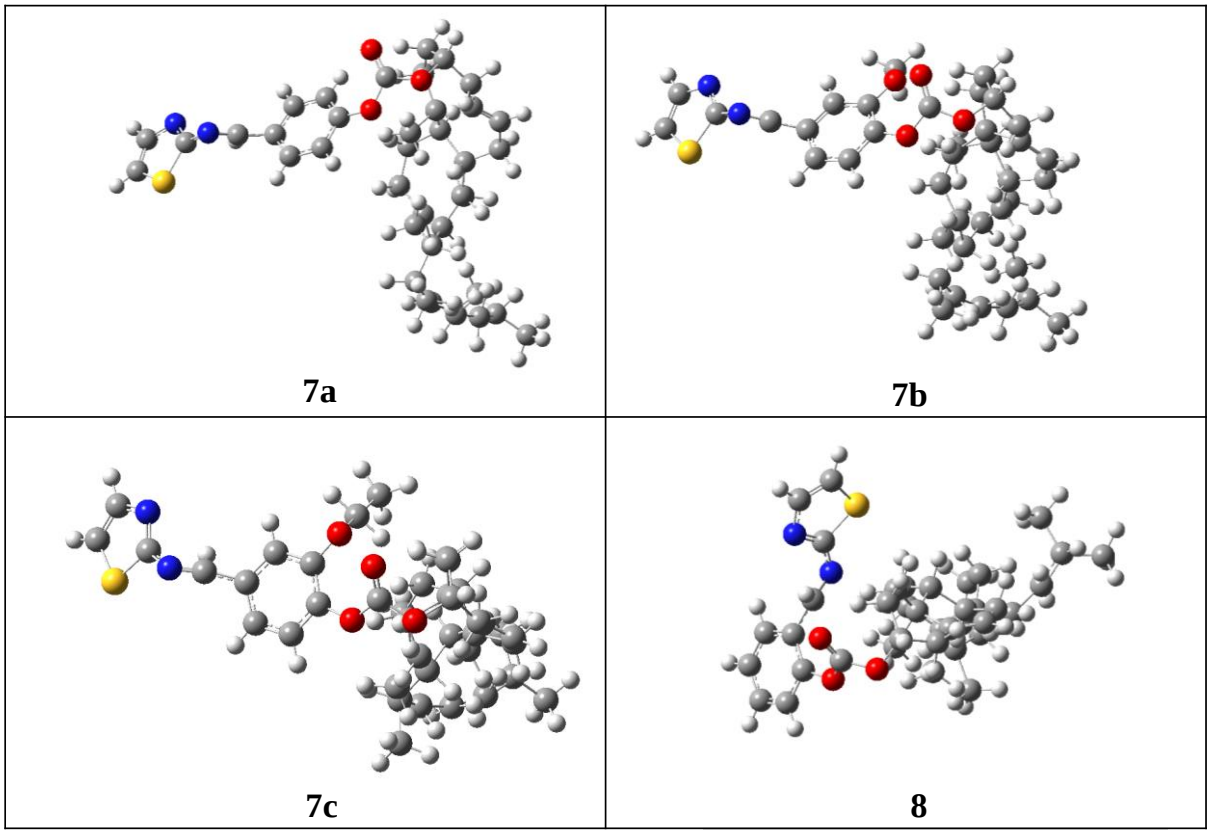

Figure 6.12: Optimized molecular structures of **7a-c** and **8**

Table 6.8: Optimized energies (Hartree) for compounds **7a-c** and **8**

Sample	Energy Minima (Hartree)
7a	-2211.086
7b	-2325.551
7c	-2364.509
8	-2211.037

The molecular frontier orbitals offer valuable insights into the chemical reactivity of molecules. E_{HOMO} quantifies the electron-donating capacity of the molecule, while E_{LUMO} denotes its ability to accept electrons [60]. Therefore, a larger E_{HOMO} signifies greater electron-donating capability, and a smaller E_{LUMO} indicates lower resistance to accepting electrons.

According to Pearson's "Hard and Soft Acids and Bases" concept, soft molecules have lower energy gap values ($\Delta E_{gap} = E_{LUMO} - E_{HOMO}$), are more stable, and are more reactive. [61].

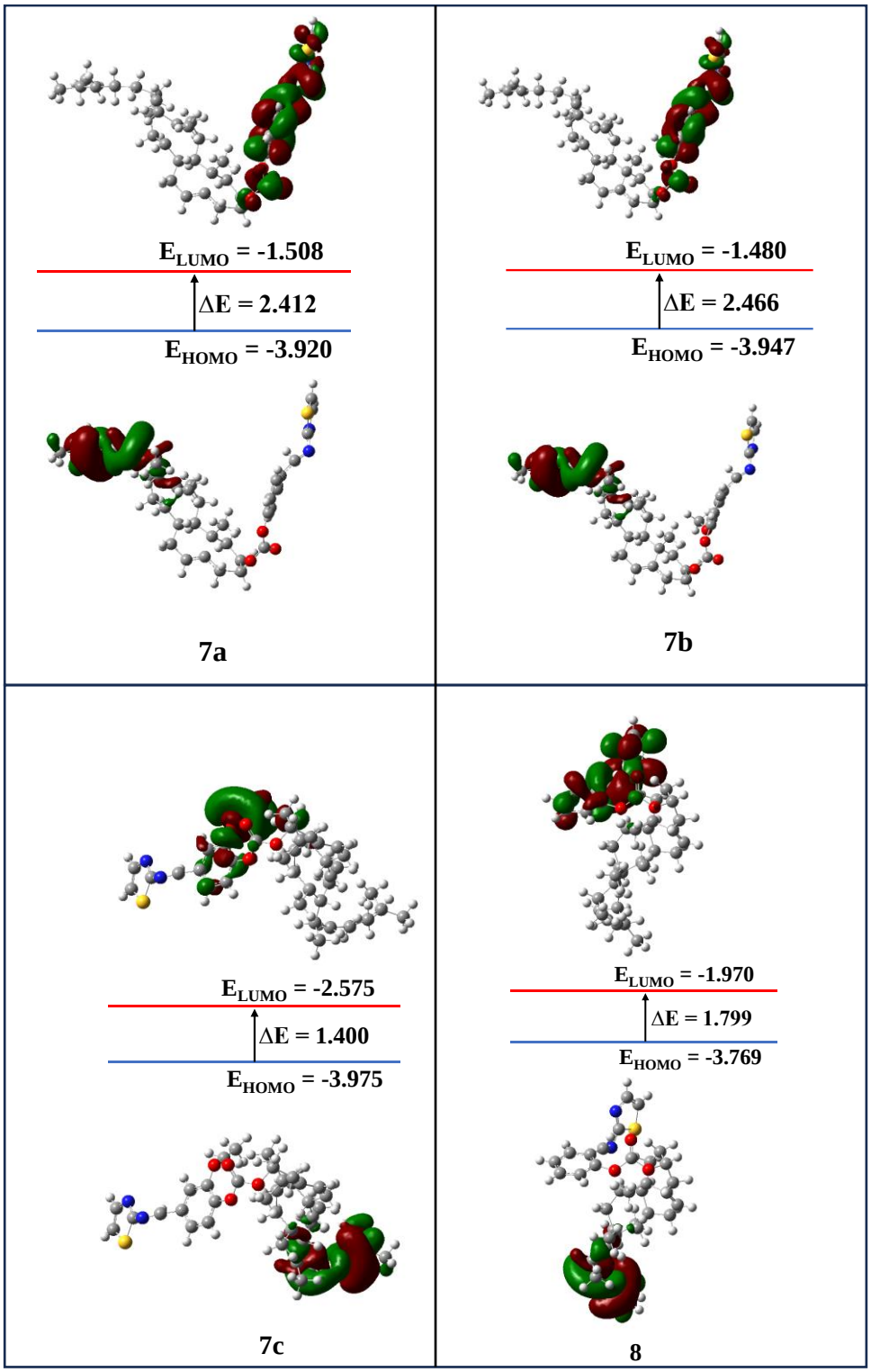

Figure 6.13: FMO contours of structures **7a-c** and **8**

Figure 6.13 displays the 3D iso surface plots of HOMO as well as LUMO, which clearly depict the composition of their atomic orbits. These plots highlight the parts of higher

and lower electron densities to provide visual illustration of the molecule's electron density distribution. The majority of electron density in the Highest Occupied Molecular Orbital (HOMO) was situated above the iso-octyl side chain of cholesterol moiety, while that of LUMO was on Schiff's base group, aromatic rings and also on thiazole ring except for molecule **7c** in which it was mainly focused on the laterally substituted ethoxy group of central phenyl ring. As shown in **Table 6.9**, the ranking of the compounds (**7a-c** and **8**) with respect to their electron-accepting capability: **7c** > **8** > **7a** > **7b**, respectively. Also, from **Table 6.9** calculations it was concluded that the reactivity of the compounds (**7a-c** and **8**) decreased in the following order: **7c** > **8** > **7a** > **7b**, respectively. The corresponding energy gap as well as E_{LUMO} for the compound **7c** was 1.400 and -2.575 eV, respectively.

Frontier MO energies and other chemical reactivity values of the optimized molecular structures are presented in **Table 6.9** [26].

Table 6.9: Molecular properties calculated using DFT for compounds **7a-c** and **8**

Sample	E_{HOMO} (eV)	E_{LUMO} (eV)	ΔE (eV)	η Global hardness	$\delta = 1/\eta$ Global softness	μ_{el} (eV)	ω Electrophilicity index
7a	-3.920	-1.508	2.412	1.20	0.83	-2.71	6.11
7b	-3.947	-1.480	2.466	1.23	0.81	-2.71	5.97
7c	-3.975	-2.575	1.400	0.70	1.43	-3.28	15.32
8	-3.769	-1.970	1.799	0.90	1.12	-2.87	9.15

As evident from **Table 6.9**, compounds exhibit chemical potentials spanning between -2.71 and -3.28 eV with highest μ_{el} for **7c** and hardness values between 0.70 to 1.23 eV, lowest for **7c**. Therefore, the compound **7c** is softer and more reactive than the other compounds of the series. Compounds' biological activity may be influenced by a significant charge-transferring interactions. The electrophilicity index measures a species' electron-accepting tendency [27]. A higher index suggests a greater attraction for electrons from a donor, with good nucleophiles having low ω values and good electrophiles possessing high ω values. It is clear from **Table 6.9** that the molecule **7c** had highest electrophilicity index values showing its good electrophilic nature.

Table 6.10: Dipole moment for **7a-c** and **8**

Sample	μ_x	μ_y	μ_z	Dipole Moment μ_{dip} (Debye)
7a	-2.0016	0.4330	0.1829	2.0560
7b	-2.2967	1.6478	-0.6326	2.8966
7c	3.6932	1.1555	1.0875	4.0197
8	1.5736	-0.1724	-0.7418	1.7482

The dipole moment components (μ_x, μ_y, μ_z) and modulus (μ_{dip}) for either compound estimated in three cartesian vectors are displayed in **Table 6.10**. The ranges of "μx, μy, and μz" were determined to lie between 1.5-3.6 D, 0.1-1.6 D, and 0.7-1.0 D, respectively. Based on their estimated values, the molecules appear to align with longer axis lying parallel to the mesophase director, since the X-axis dipole moment component is larger than the transverse axis.

6.3.8.2. Molecular Electrostatic Potential (MEP)

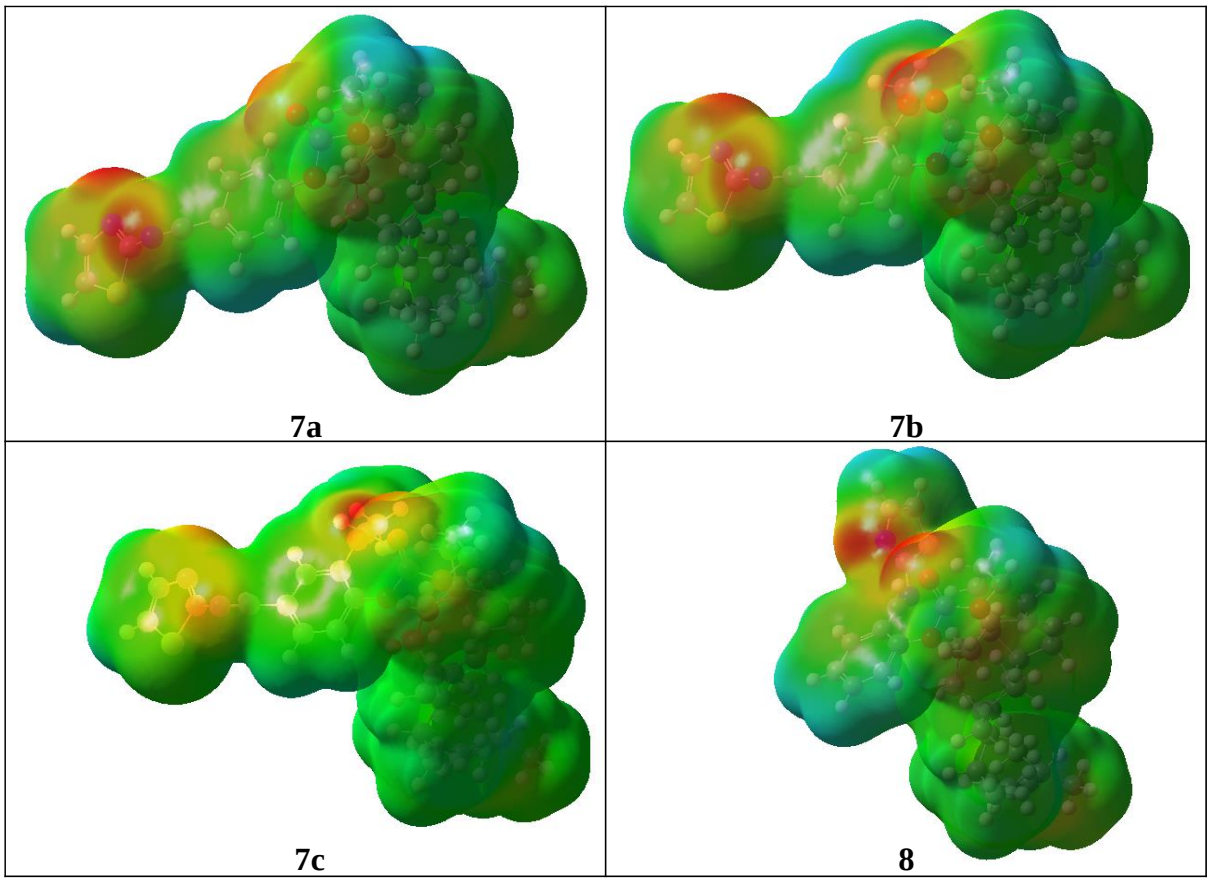

Figure 6.14: Molecular electrostatic potentials (MEP) for the compounds **7a-c** and **8**

"Molecular electrostatic potential" (MEP) maps are an advantageous tool designed for understanding intermolecular interactions, sites of electrophilic attack and nucleophilic reactions, and values for iso-surface with the site of positive as well as negative electrostatic potentials [62]. For drug design, MEP maps are useful for assessing binding locations depending on how a particular molecule recognizes another [63]. In order to determine the most likely sites for the interaction of molecules with both electrophilic and nucleophilic species, MEP was computed at the optimised geometry of B3LYP-6-31G (d, p). Different colours indicated surface electrostatic potential levels. In **Figure 6.14**, the red represents the highest electronegative electrostatic potential, blue the most positive, and green zero potential. The N atoms of thiazole and Schiff's base have a larger negatively charged surface; expect for compound **7c** in which it was intensive over the laterally substituted ethoxy group of central phenyl ring. Thus, electrophilic attack may be easier on these sites and should bind to active drug-receptor sites.

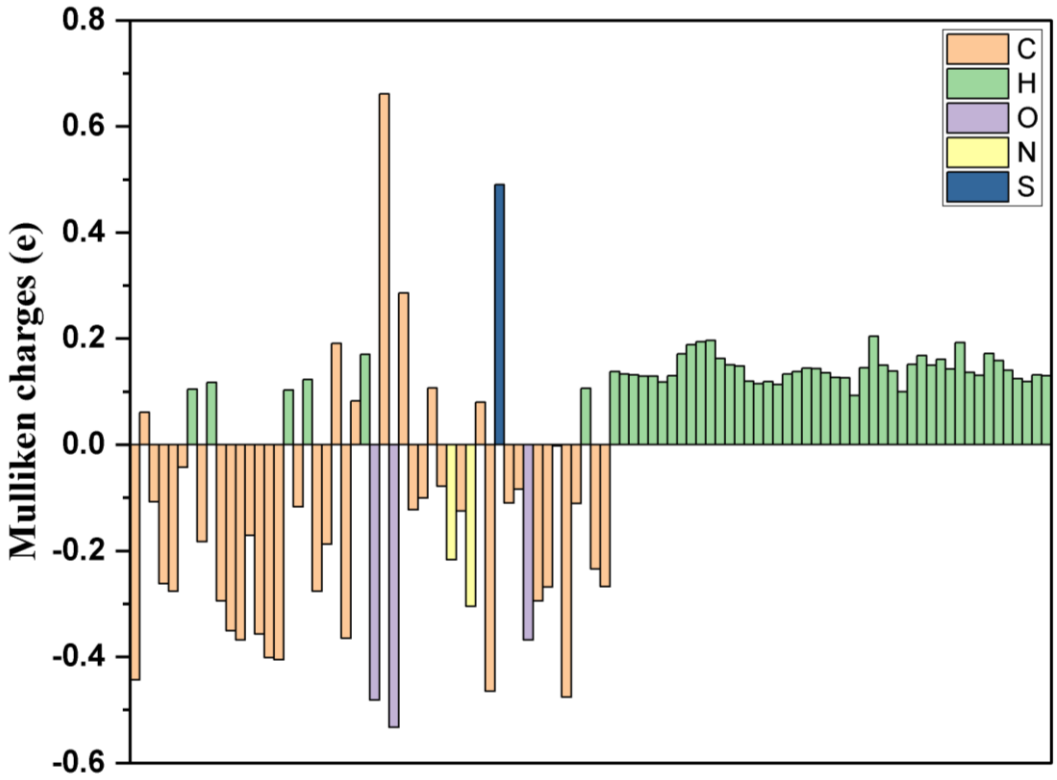

Figure 6.15: Mulliken charges of compound **7a**

The greater positive and negative atomic charge values in 7a indicates a higher tendency for LC nature of the molecule. [64]. Thus, the distribution of mulliken's atomic charge in **7a** is critical in establishing its mesomorphic nature, The distribution of Mulliken's atomic charge in **7a** is crucial in determining its LC nature, where oxygen atoms carry a greater negative charge

and hydrogen, carbon, and sulphur atoms possessing a stronger positive charge. **Figure 6.15** illustrates the atomic charge distribution of **7a**.

6.4. Conclusion

In conclusion, four new Schiff's bases were synthesised by condensing 2-amino-1,3-thiazole with four different substituted formyl phenyl cholesteryl carbonates and were investigated for their anti-microbial, anti-oxidant, mesogenic, optical and thermal properties as well. While the compounds did not exhibit better radical scavenging activity as compared to standard, all the derivatives demonstrated significant to moderate levels of antibacterial and antifungal activities. Out of the four derivatives only one derivative **7a** (without substituted core) was shown to possess mesogenic property showing chiral nematic mesophase (N*). All the derivatives were UV active and also exhibit photoluminescence in blue emission spectrum as well. Thermal analysis result indicates that slight change in molecular structures, changes the overall thermal stability of resultant molecule. The derivatives show moderate drug-likeness and bioactivity score. Theoretical chemical reactivity studies, considering the Frontier MOs and MEP mapping, predicted the high and low electron density areas highlighting the potential interacting sites of molecules for biological activity and the higher value of positive and negative atomic charge for confirming the liquid crystalline property.

6.5. References

[1] Kabir E, Uzzaman M. A review on biological and medicinal impact of heterocyclic compounds. Results Chem. 2022;**4**:100606.

[2] Sapra R, Patel D, Meshram D. A mini review: recent developments of heterocyclic chemistry in some drug discovery scaffolds synthesis. J Med Chem Sci. 2020;**3**:71–78.

[3] Jampilek J. Heterocycles in Medicinal Chemistry. Molecules. 2019;**24**:3839.

[4] Kerru N, Gummidi L, Maddila S, et al. A Review on Recent Advances in Nitrogen-Containing Molecules and Their Biological Applications. Molecules. 2020;**25**:1909.

[5] Smith BR, Eastman CM, Njardarson JT. Beyond C, H, O, and N! Analysis of the Elemental Composition of U.S. FDA Approved Drug Architectures. J Med Chem. 2014;**57**:9764–9773.

[6] Aljamali NM, Alfatlawi IO. Synthesis of Sulfur Heterocyclic Compounds and Study of Expected Biological Activity. Res J Pharm Technol. 2015;**8**:1225–1242.

[7] Pathania S, Narang RK, Rawal RK. Role of sulphur-heterocycles in medicinal chemistry: An update. Eur J Med Chem. 2019;**180**:486–508.

[8] Scott KA, Njardarson JT. Analysis of US FDA-Approved Drugs Containing Sulfur Atoms. Top Curr Chem. 2018;**376**:5.

[9] Kaye PT, Musa MA, Nchinda AT, et al. Novel Heterocyclic Analogues of the HIV-1 Protease Inhibitor, Ritonavir. Synth Commun. 2004;**34**:2575–2589.

[10] Dash AK. Tolnaftate. In: Brittain HG, editor. Anal Profiles Drug Subst Excip [Internet]. Academic Press; 1994. p. 543–570. Available from: https://www.sciencedirect.com/science/article/pii/S0099542808606127.

[11] Hantzsch A, Weber JH. Ueber Verbindungen des Thiazols (Pyridins der Thiophenreihe). Berichte Dtsch Chem Ges. 1887;**20**:3118–3132.

[12] Moradi AV, Peyghan AA, Hashemian S, et al. Theoretical Study of Thiazole Adsorption on the (6,0) zigzag Single-Walled Boron Nitride Nanotube. Bull Korean Chem Soc. 2012;**33**:3285–3292.

[13] Pola S. Significance of Thiazole-based Heterocycles for Bioactive Systems. Scope Sel Heterocycles Org Pharm Perspect [Internet]. IntechOpen; 2016. Available from: https://www.intechopen.com/chapters/49951.

[14] Farouk Elsadek M, Mohamed Ahmed B, Fawzi Farahat M. An Overview on Synthetic 2-Aminothiazole-Based Compounds Associated with Four Biological Activities. Molecules. 2021;**26**:1449.

[15] Ibraheem TK, Karam NH, Al-Dujaili AH. Synthesis and characterization of symmetrical liquid crystalline compounds based on oxazole and thaizole rings. Mol Cryst Liq Cryst. 2020;**710**:1–12.

[16] Lee C-H, Yamamoto T. Synthesis of Liquid Crystals with Bent-Rod Structure: Mesogenic Thiazole Derivatives with Long Alkoxyl Chains. Mol Cryst Liq Cryst Sci Technol Sect Mol Cryst Liq Cryst. 2001;**363**:77–84.

[17] Kotian SY, Mohan CD, Merlo AA, et al. Small molecule based five-membered heterocycles: A view of liquid crystalline properties beyond the biological applications. J Mol Liq. 2020;**297**:111686.

[18] Santos ABS, Manfredi AM, Salla CAM, et al. Highly luminescent liquid crystals by connecting 1,3,4-oxadiazole with thiazolo[5,4-d]thiazole units. J Mol Liq. 2021;**321**:114887.

[19] Schneider JMFM, Sales ES, Livotto PR, et al. Synthesis of New Family of Thiazoline and Thiazole Esters and Investigation of their Thermal Properties. J Braz Chem Soc. 2014;**25**:1493–1503.

[20] Albuquerque HMT, Santos CMM, Silva AMS. Cholesterol-Based Compounds: Recent Advances in Synthesis and Applications. Molecules. 2019;**24**:116.

[21] Bairwa SK, Sonera SA, Tandel RC. Cholesterol based mesogenic Schiff's base derivatives with carbonate linkage: Synthesis, characterisation and photoluminescence study. Liq Cryst. 2023;**50**:2495–2509.

[22] Paduch R, Woźniak A. The Effect of Lamium album Extract on Cultivated Human Corneal Epithelial Cells (10.014 pRSV-T). J Ophthalmic Vis Res. 2015;**10**:229–237.

[23] Mukhia R, Basistha B, Chhetri DR. Variation in Antioxidant Activity of a Rattan Species, Plectocomia himalayana Griff. by DPPH assay based on two different methods of Methanol Extraction. Res J Pharmacogn Phytochem. 2018;**10**:175–178.

[24] Gupta AK, Kalpana S, Malik JK. Synthesis and In Vitro Antioxidant Activity of New 3-Substituted-2-Oxindole Derivatives. Indian J Pharm Sci. 2012;**74**:481–486.

[25] Frisch M, Trucks G, Schlegel H, et al. Gaussian 09 (Revision A02). Gaussian Inc Wallingford CT. 2009;

[26] Pearson RG. Chemical hardness and the electronic chemical potential. Inorganica Chim Acta. 1992;**198–200**:781–786.

[27] Islam N, Ghosh DC. On the Electrophilic Character of Molecules Through Its Relation with Electronegativity and Chemical Hardness. Int J Mol Sci. 2012;**13**:2160–2175.

[28] Salihović M, Pazalja M, Špirtović Halilović S, et al. Synthesis, characterization, antimicrobial activity and DFT study of some novel Schiff bases. J Mol Struct. 2021;**1241**:130670.

[29] Lemilemu F, Bitew M, Demissie TB, et al. Synthesis, antibacterial and antioxidant activities of Thiazole-based Schiff base derivatives: a combined experimental and computational study. BMC Chem. 2021;**15**:67.

[30] Chandrasekhar S. Liquid Crystals [Internet]. 2nd ed. Cambridge: Cambridge University Press; 1992. Available from: https://www.cambridge.org/core/books/liquid-crystals/7972CBEB90A0F90F0D23C9B83B6A46D2.

[31] Kulkarni C, Di Nuzzo D, Meijer EW, et al. Pitch and Handedness of the Cholesteric Order in Films of a Chiral Alternating Fluorene Copolymer. J Phys Chem B. 2017;**121**:11520–11527.

[32] Taugerbeck A, Booth CJ. Design and Synthesis of Chiral Nematic Liquid Crystals. Handb Liq Cryst [Internet]. John Wiley & Sons, Ltd; 2014. p. 1–63. Available from: https://onlinelibrary.wiley.com/doi/abs/10.1002/9783527671403.hlc053.

[33] Petrov VF, Tasaka T, Okamoto H, et al. The Influence of Lateral Substitution of Liquid Crystals on the Structure of their Smectic Ad Phases. Mol Cryst Liq Cryst Sci Technol Sect Mol Cryst Liq Cryst. 2000;**338**:11–20.

[34] Zhou M, Zhang J, Wang S, et al. Laterally substituted ionic liquid crystals and the resulting rheological behavior. Soft Matter. 2012;**8**:7945–7951.

[35] Ahmed NHS, Saad GR, Naoum MM. Effect of position of the lateral fluoro substituent on the mesophase behaviour of aryl 4-alkoxyphenylazo benzoates in pure and binary mixtures. Liq Cryst. 2018;**45**:1487–1497.

[36] Ahmed HA, Khushaim MS. Nematogenic Laterally Substituted Supramolecular H-Bonded Complexes Based on Flexible Core. Crystals. 2020;**10**:878.

[37] Weissflog W. Laterally Substituted and Swallow-Tailed Liquid Crystals. Handb Liq Cryst Set [Internet]. John Wiley & Sons, Ltd; 1998. p. 835–863. Available from: https://onlinelibrary.wiley.com/doi/abs/10.1002/9783527619276.ch8c.

[38] Karipcin F, Kabalcilar E, Ilican S, et al. Synthesized some 4-(2-thiazolylazo)resorcinol complexes: Characterization, thermal and optical properties. Spectrochim Acta A Mol Biomol Spectrosc. 2009;**73**:174–180.

[39] Liu H, Fu Z, Xu K, et al. Structure–Property Relationship of Highly π-Conjugated Schiff-Base Moiety in Liquid Crystal Diepoxide Polymerization and Mesophases Stabilization. J Phys Chem B. 2011;**115**:7568–7577.

[40] Sharma BP, Subin JA, Marasini BP, et al. Triazole based Schiff bases and their oxovanadium(IV) complexes: Synthesis, characterization, antibacterial assay, and computational assessments. Heliyon. 2023;**9**:e15239.

[41] Ma S-Y, Zhi Y-S, Zhang H-S, et al. Fluorescent cholesteric liquid crystal polymers with dual properties: design, synthesis and characterisation. Liq Cryst. 2023;1–15.

[42] Taylor AT, Lai EPC. Current State of Laser-Induced Fluorescence Spectroscopy for Designing Biochemical Sensors. Chemosensors. 2021;**9**:275.

[43] Jiang J, Gill BS. Current status and the future of fluorescence in situ hybridization (FISH) in plant genome research. Genome. 2006;**49**:1057–1068.

[44] Kobayashi H, Ogawa M, Alford R, et al. New Strategies for Fluorescent Probe Design in Medical Diagnostic Imaging. Chem Rev. 2010;**110**:2620–2640.

[45] Yadollahpour, Ali, Rezaee, Zohre, Jalilifar, Mostafa, et al. Dye-Doped Fluorescent Nanoparticles in Molecular Imaging: A Review of Recent Advances and Future Opportunities. Material Science Research India [Internet]. 2014;**11**:2. Available from: http://www.materialsciencejournal.org/vol11no2/dye-doped-fluorescent-nanoparticles-in-molecular-imaging-a-review-of-recent-advances-and-future-opportunities/.

[46] Flusberg BA, Cocker ED, Piyawattanametha W, et al. Fiber-optic fluorescence imaging. Nat Methods. 2005;**2**:941–950.

[47] Chu C-S, Lo Y-L, Sung T-W. Review on recent developments of fluorescent oxygen and carbon dioxide optical fiber sensors. Photonic Sens. 2011;**1**:234–250.

[48] Jebapriya JC, Jonathan DR, Kirupavathy SS, et al. Growth and characterization of a cyclohexanone based chalcone crystal 2(E)-(4-N,N-dimethylaminobenzylidene)-5-methylcyclohexanone for nonlinear optical applications. Opt Mater. 2020;**107**:110035.

[49] Lin L, Rong M, Luo F, et al. Luminescent graphene quantum dots as new fluorescent materials for environmental and biological applications. TrAC Trends Anal Chem. 2014;**54**:83–102.

[50] Bonifácio VDB, Correia VG, Pinho MG, et al. Blue emission of carbamic acid oligooxazoline biotags. Mater Lett. 2012;**81**:205–208.

[51] Leeson PD, Davis AM, Steele J. Drug-like properties: guiding principles for design – or chemical prejudice? Drug Discov Today Technol. 2004;**1**:189–195.

[52] Lipinski CA, Lombardo F, Dominy BW, et al. Experimental and computational approaches to estimate solubility and permeability in drug discovery and development settings1PII of original article: S0169-409X(96)00423-1. The article was originally published in Advanced Drug Delivery Reviews 23 (1997) 3–25.1. Adv Drug Deliv Rev. 2001;**46**:3–26.

[53] Ariffin A, Rahman NA, Yehye WA, et al. PASS-assisted design, synthesis and antioxidant evaluation of new butylated hydroxytoluene derivatives. Eur J Med Chem. 2014;**87**:564–577.

[54] Wang R, Fu Y, Lai L. A New Atom-Additive Method for Calculating Partition Coefficients. J Chem Inf Comput Sci. 1997;**37**:615–621.

[55] Wani MY, Bhat AR, Azam A, et al. Nitroimidazolyl hydrazones are better amoebicides than their cyclized 1,3,4-oxadiazoline analogues: In vitro studies and Lipophilic efficiency analysis. Eur J Med Chem. 2013;**64**:190–199.

[56] Hartung IV, Huck BR, Crespo A. Rules were made to be broken. Nat Rev Chem. 2023;**7**:3–4.

[57] Verma A. Lead finding from Phyllanthus debelis with hepatoprotective potentials. Asian Pac J Trop Biomed. 2012;**2**:S1735–S1737.

[58] Leach AR. Molecular modelling- PRINCIPLES AND APPLICATIONS. 2nd edition. England: Pearson Education Limited; 2001.

[59] Kryachko ES, Ludeña EV. Energy Density Functional Theory of Many-Electron Systems [Internet]. Dordrecht: Springer Netherlands; 1990. Available from: http://link.springer.com/10.1007/978-94-009-1970-9.

[60] Miar M, Shiroudi A, Pourshamsian K, et al. Theoretical investigations on the HOMO–LUMO gap and global reactivity descriptor studies, natural bond orbital, and nucleus-independent chemical shifts analyses of 3-phenylbenzo[d]thiazole-2(3H)-imine and its para-substituted derivatives: Solvent and substituent effects. J Chem Res. 2021;**45**:147–158.

[61] Pearson RG. Hard and Soft Acids and Bases. J Am Chem Soc. 1963;**85**:3533–3539.

[62] Suresh Kumar GS, Antony Muthu Prabu A, Jegan Jenniefer S, et al. Syntheses of phenoxyalkyl esters of 3,3′-bis(indolyl)methanes and studies on their molecular properties from single crystal XRD and DFT techniques. J Mol Struct. 2013;**1047**:109–120.

[63] Raha K, Peters MB, Wang B, et al. The role of quantum mechanics in structure-based drug design. Drug Discov Today. 2007;**12**:725–731.

[64] Sharma D, Tiwari G, Tiwari SN. Electronic and electro-optical properties of 5CB and 5CT liquid crystal molecules: A comparative DFT study. Pramana. 2021;**95**:71.